# Implementation and Demonstration of a Time Domain Modeling Tool for Floating Oscillating Water Columns

Wendelle F. Sparrer

Thesis submitted to the Faculty of the
Virginia Polytechnic Institute and State University
in fulfillment of the requirements for the degree of

Master of Science
in
Mechanical Engineering

Pablo A. Tarazaga, Chair
Blake C. Boren
Andrew Kurdila

December 8, 2020
Blacksburg, Virginia

Keywords: Wave Energy Harvesting, Oscillating Water Column, Time Domain Simulation, BBDB

# Implementation and Demonstration of a Time Domain Modeling Tool for Floating Oscillating Water Columns

Wendelle F. Sparrer

(ABSTRACT)

Renewable energy is a critical component in combating climate change. Ocean wave energy is a source of renewable energy that can be harvested using Wave Energy Converters (WECs). One such WEC is the floating Oscillating Water Column (OWC), which has been successfully field tested and warrants further exploration. This research implements a publicly accessible code in MatLab and SimuLink to simulate the dynamics of a floating OWC in the time domain. This code, known as the Floating OWC Iterative Time Series Solver (FlOWCITSS), uses the pressure distribution model paired with state space realization to capture the internal water column dynamics of the WEC and estimate pneumatic power generation. Published experimental results of floating moored structures are then used to validate FlOWCITSS. While FlOWCITSS seemed to capture the period and general nature of the heave, surge, and internal water column dynamics, the magnitude of the most important responses sometimes had errors ranging from $1.5\% - 37\%$. This error could be caused by the modeling techniques used, or it could be due to uncertainties in the experiments. The presence of smaller error values shows potential for FlOWCITSS to achieve consistently higher fidelity results as the code undergoes further developments. To demonstrate the use of FlOWCITSS, geometry variations of a Backward Bent Duct Buoy (BBDB) are explored for a wave environment and mooring configuration. The reference model from Sandia National Labs, RM6, performed significantly better than a BBDB with an altered stern geometry for a 3 second wave period, indicating that stern geometry can have a significant impact on pneumatic power performance.

# Implementation and Demonstration of a Time Domain Modeling Tool for Floating Oscillating Water Columns

Wendelle F. Sparrer

## (GENERAL AUDIENCE ABSTRACT)

Renewable energy is a critical component in combating climate change. Ocean wave energy is a source of renewable energy that can be converted into electricity using Wave Energy Converters (WECs). One such WEC is the floating Oscillating Water Column (OWC), which has been successfully field tested and warrants further exploration. Floating OWCs are partially submerged floating structures that have an internal chamber which water oscillates in. The motions of the water displace air inside this chamber, causing the air to be forced through a high speed turbine, which generates electricity. This research develops a publicly accessible code using MatLab and SimuLink to evaluate the motions and power generation capabilities of floating OWCs. This code is then validated against physical experiments to verify its effectiveness in predicting the device's motions. This publicly accessible code, known as the Floating OWC Iterative Time Series Solver (FlOWCITSS), showed error ranging from $1.5\% - 37\%$ for the most important motions that are relevant to energy harvesting and power generation. These errors could be caused by the numerical models used, or uncertainties in experimental data. The presence of smaller error values shows potential for FlOWCITSS to achieve consistently higher fidelity results as the code undergoes further developments. To demonstrate the use of FlOWCITSS, geometry variations of floating OWCs are explored.

# Acknowledgments

I want to first thank my advisor, Dr. Pablo Tarazaga, whose patience, support, and humor acted as a balm for the challenges I faced over the course of my research. Dr. Tarazaga fosters a rich community, and his dedication to doing so has been warming and inspirational. I would also like to thank Dr. Blake Boren, without whom I would likely not be where I am right now. His expertise in wave energy has pushed me to be a better engineer, and his kindness and candid acceptance helped create an environment where I could thrive. Additionally, I would like to express my gratitude for Dr. Andrew Kurdila, who volunteered his time to be on my committee.

I am grateful for my lab mates, whose company, friendly support, and camaraderie were a source of joy. Special thanks to Dr. Jeremy Kolansky for helping review my thesis and to Sheyda Davaria for listening to my SimuLink woes. I would also like to extend my gratitude to Professor Robin Ott and Melissa Williams for listening to me and providing me with guidance when I needed it most. Additionally, I would like to express my immense appreciation for the Cook Counseling Center, Dr. Trent Davis, and Moose the therapy dog for helping me during my time at Virginia Tech.

I would also like to thank Minghao Wu from the University of Ghent, who was kind enough to share his experimental data with me and answer my questions. His data was instrumental in troubleshooting and testing my modeling tool, especially since experimentally testing physical geometries was inaccessible to me in my research.

Thank you to my parents for their support and love during my pursuit for higher education, and thank you to my partner, Conor, and my friends, Gabby and Diana, for the emotional support and laughs over the course of my degree.

Finally I would like to thank Dr. Lei Zuo for introducing me to wave energy and giving me an opportunity to learn about this exciting field. He was instrumental in helping me get the Powell Graduate Fellowship, which funded my first year of my graduate education. I would like to extend this appreciation to the Virginia Tech Graduate School for awarding me the Powell Graduate Fellowship, which gave me the opportunity to pursue a topic that mattered to me.

# Contents

# List of Figures

# List of Tables

# Chapter 1

# Introduction and Literature Review

## 1.1 Research Motivation

There is a global dependence on fuels, such as coal and natural gas, that release greenhouse gases (GHG), like carbon and methane, into the atmosphere. These GHG emissions are a direct driver of climate change, which is an urgent issue that affects the planet [17]. In order to properly mitigate the devastating effects of climate change, it is imperative to phase out sources of energy that create these greenhouse gases. One path forward for doing this is by electrifying different sectors, such as transportation and industry, and then decarbonizing electricity [45]. This would result in an increased need for renewable energy world wide. Many forms of renewable energy are available, such as wind, solar, geothermal, hydrokinetic, and ocean wave energy.

There is around 2640 TWh/yr available in wave energy along the United States coastal shelf, and Wave Energy Converters (WECs) have the potential to capture some of that power to supply coastal regions with electricity [18]. While WECs are technically feasible, they are not yet economically feasible [1]. Economic feasibility is affected by several aspects of the WEC, such as survivability, efficiency, cost of development, and cost of maintenance [1]. Traits in a WEC that could improve survivability are a minimal number of moving parts and a design that has no hard stops, criteria which suggest that an Oscillating Water Column (OWC) is a promising device archetype to further develop. OWCs have a partially submerged shaft that a column of water oscillates in, causing an air pressure differential in the shaft that pushes air through a turbine at the top of the shaft, which turns and generates electricity.

Several OWC archetypes exist, one of them being the floating Backward Bent Duct Buoy (BBDB) OWC, which has the benefit of taking advantage of motion in multiple degrees of freedom in order to generate power [25]. However, the motion in these degrees of freedom is complexly coupled, making it challenging to analytically assess how changes in the structure of the device could impact performance [37]. Several studies have evaluated how device structure can affect BBDB performance, such as a 2D study done by Suzuki, and a frequency domain parametric study conducted by Portillo [33, 41]. While these studies have evaluated how device geometry affects WEC performance, none of them have evaluated how the three dimensional device geometry impacts performance in the time domain. Time domain modeling of WECs is important because of the nonlinear effects that OWC WECs are subjected to, such as viscous drag, air compressibility, turbine dynamics, and mooring forces and damping [19]. Exploring how hull geometry impacts device performance in the time domain could help improve the efficiency of these devices, and therefore the economic feasibility of these devices. Therefore, this thesis seeks to explore different hull geometries of floating OWCs to evaluate their impact on performance.

The process of modeling OWC WECs in the time domain is intensive, since many dynamics can be considered, such as mooring, drag, added mass and radiation damping, water column dynamics, air compressibility, turbine dynamics, and the ocean wave inputs to the system. A free modeling tool has been released by Sandia National Labs and NREL called WECSim, which can model many WECs in the time domain, but is only able to model fixed OWC devices, not floating OWCs [39]. There are also licensed softwares that can be used to assess time domain device dynamics, such as Proteus DS and Orcaflex. Additionally, these modeling tools do not use the pressure distribution model, which considers the variation of water velocity inside the internal water column and is theoretically better suited to larger WECs [30]. However, no free numerical modeling tool has been developed and released to the public to evaluate floating OWCs in the time domain. Since floating OWCs are a promising avenue of ocean wave energy production, the existence of a lower cost option to evaluate structures in the time domain could help accelerate the innovations to this particular WEC archetype. Therefore, this research seeks to develop and release a version of this tool.

In implementing a time domain modeling tool for OWCs, it is important to accurately capture the internal water column dynamics, since they are complexly paired with the body motion of the device. The time domain modeling tool generates Frequency Response Functions (FRFs) that capture the dynamics of the internal water surface and how they couple with body motion. State space realization using frequency domain identification and FRFs has been previously shown to accurately approximate body dynamics in the time domain, but not internal water column dynamics using the pressure distribution model [24, 32]. This body of work demonstrates that a state space realization of the internal water column FRFs adequately represents the dynamics of the device in the time domain.

## 1.2 Overview of Wave Energy Converters

Wave Energy Converters (WECs) are devices that convert mechanical energy from ocean waves into usable power. The system in a WEC that converts energy into usable power is the Power Take-Off (PTO) system. Many types of WECs exist, designed to operate in numerous environments and harvest wave energy in different ways. Unsurprisingly, WECs can be classified using several measures, from their size to their proximity to the shore [1].

A WEC's proximity to shore determines many design elements. If a device is off-shore, special consideration must be had for how the energy is going to get back to land and how the devices are to be consistently maintained [8]. Devices that are near shore or on the shore are simpler when it comes energy transport, but the waves near shore tend to be smaller, which can limit the capabilities of these devices.

One of the most prominent distinctions between devices is between their ”working principles”, or how they physically capture the energy from the waves [8]. Falcão identified three primary working principles that most WECs fall under: oscillating bodies, overtopping devices, and Oscillating Water Columns (OWCs) [8]. The broadest group of WECs is the oscillating body group. These devices include floating heaving buoys, two mass heaving systems, pitching devices, bottom-moored clam shell devices, and multi-body systems [8]. These devices rely on body motion in one or more degrees of freedom to harvest energy from ocean waves. This is distinct from the overtopping devices, which are fixed. Overtopping devices are stationed close to shore and are positioned to capture water from waves and store the water above the average water line, taking advantage of potential energy. When the water is released, it flows through a turbine, which generates electricity [8]. Overtopping devices and OWCs are similar in that they both use turbines to generate electricity. The difference between them is that while overtopping devices actuate the turbine with water, OWCs actuate the turbine with air. OWCs are structures, floating or fixed, with inner chambers that are partially submerged. When water from incoming waves oscillates in these chambers, air is compressed inside the chamber and is forced through a turbine, generating electricity [11]. These dynamics are demonstrated in Figure 1.1, where a turbine would be placed across the opening to the atmosphere.

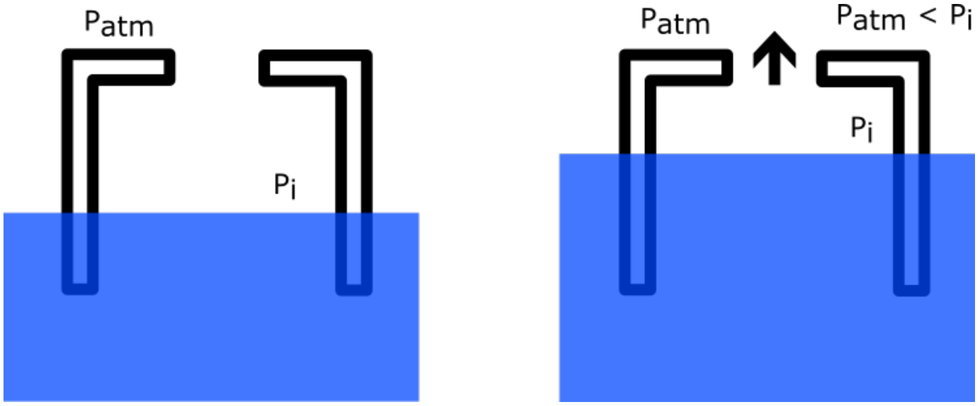

Figure 1.1: Demonstration of how oscillations in wave height compress the air and force it through an opening to the atmosphere. $P_i$ represents the pressure inside the air chamber and $P_{atm}$ represents the atmospheric pressure.

## 1.3 Overview of Oscillating Water Columns

OWCs are a very promising WEC design, since they have several benefits over WECs in other categories. Firstly, the PTO system in an OWC is a turbine, which has no hard stops, which theoretically increases survivability [1]. Some WECs, like a two mass heave system, might have a PTO in the form of a ball screw that rotates a generator in response to motion in one degree of freedom. This ball screw has a hard stop at the ends of the screw, which can limit device life if it experiences fatigue. A turbine does not have the same issue, since it's a purely rotational PTO. Secondly, OWCs are able to convert low frequency inputs into power through the use of high speed air turbines [12]. These benefits have resulted in a focus on OWCs in the wave energy community and several successful field tests. One such field test is of the Mighty Whale, a floating offshore OWC tested off the shores of Japan by Washio and Osawa in 1998 [44]. Their field test helped prove the technical feasibility of OWC devices in a real ocean environment.

Not all OWCs are the same; they can be further categorized into fixed or floating structures. Fixed OWCs are stationary in the water and the only power generation comes from the movement of the water in the internal device chamber. Floating OWCs are capable of movement themselves, so the power generation is caused by the relative movement between the water column and the floating structure. There are many different kinds of floating OWCs, one of the oldest being the spar-buoy [8]. This structure is essentially a floating buoy whose internal water column is a vertical cylinder, with an opening at the bottom of the buoy and an opening above the surface of the water where a turbine would be placed for power generation. This device has substantial drag due to its basic geometry, thus in the 1980s, Masuda conceived of the floating Backward Bent Duct Buoy (BBDB) OWC [25]. This structure has lower drag than the spar-buoy device and can be deployed in shallower waters [25]. Furthermore, the BBDB enables a longer water column chamber, which helps the floating device tune to the frequency of incoming waves [8]. The BBDB has been developed since its conception in the 1980s. Sandia National Labs included the BBDB in its Reference Model Project for WECs, which intended to document major WEC archetypes and evaluate them for different metrics, which could be used as benchmarks to evaluate improvements in marine and hydrokinetic power [4]. Reference Model 6 (RM6), shown in Figure 1.2, is the identifier given to the BBDB. This body of research will use RM6 as a starting point for hull geometry exploration, since it has been rigorously studied and is intended to be used as a benchmark.

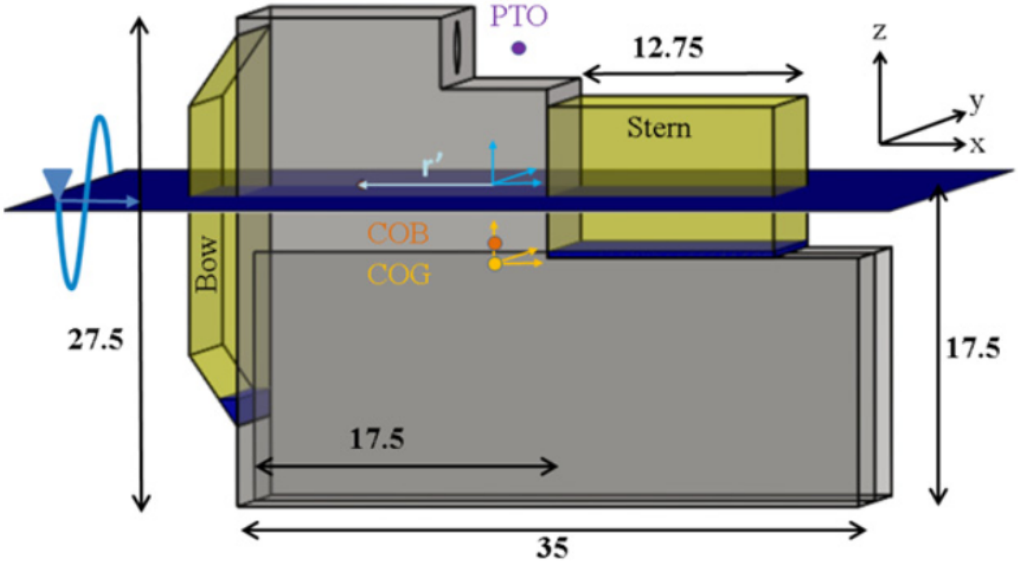

Figure 1.2: Reference Model 6, designed in the Reference Model Project by Sandia National Labs and the Department of Energy [4]

Bull calculated the average annual pneumatic power output of RM6 in random waves to be around 208 kW, with an annual electrical power output of 103 kW after considering an air turbine and electric generator [5]. This conversion efficiency from pneumatic to electric power is around 50%, which is fairly typical for this device archetype [36]. Pneumatic to electric conversion efficiency is dependent on the turbine and control system used. This body of work considers a turbine when modeling device dynamics, but does not focus on optimizing pneumatic to electric conversion efficiency. This work's primary concern is with the efficiency of conversion of wave power to pneumatic power. Therefore, a Well's Turbine, which is a bidirectional turbine developed with OWC devices in mind, will be considered in this work when simulating device dynamics.

The loading across the air outlet impacts the device's primary efficiency, but the primary efficiency is more heavily influenced by the body dynamics of the device, which in turn are determined by the shape of the OWC WEC. In order to determine device performance, it is critical to select an appropriate modeling strategy.

## 1.4 Modeling in the Frequency and Time Domain

There are several different modeling techniques that can be used to predict WEC performance in different wave conditions. Two common techniques are hydrodynamic analysis and Computational Fluid Dynamics (CFD). While CFD can capture dynamics caused by small changes in geometries, like rounded corners or lips on edges, it is computationally expensive and time consuming. The other technique, hydrodynamic analysis, uses potential flow theory to determine the velocity potential, body loads, and damping in the frequency domain. Hydrodynamic analysis is significantly less computationally expensive than CFD, making it convenient to use for general rigid body WEC design. For the purposes of this body of work, only hydrodynamic analysis will be used.

The general workflow for hydrodynamic analysis consists of modeling device geometry, using a program to find the hydrodynamic coefficients in the frequency domain, and then converting those hydrodynamic coefficients into FRFs. These FRFs can be used directly to model device dynamics in the frequency domain by solving a set of coupled force equations. The FRFs can also be converted to Impulse Response Functions (IRFs) using a Fourier transform, which can be used in tandem with convolution integration to predict device dynamics in the time domain [6]. Time domain hydrodynamic analysis can be fully linear, partially nonlinear, or fully nonlinear [2, 6, 28]. The ability of certain time domain models to capture nonlinear effects, such as viscous drag, mooring, and air compressibility, makes them a powerful tool to predict device dynamics in a variety of wave conditions [19]. This study uses a partially nonlinear time domain model that considers linear potential flow theory and nonlinear models for air compressibility and drag. A partially nonlinear model is used because it takes advantage of the ease of linear potential flow theory while allowing for certain traits, like drag, air compressibility, and mooring, to be considered with a more realistic nonlinear model. Additionally, certain partially nonlinear models have shown to be promising in modeling device performance [2].

Simulating devices in the time domain is more complicated than in the frequency domain. Time domain modeling requires converting the FRFs to IRFs or finding a state space representation using the FRFs. The nonlinear effects require special consideration and the use of a nonlinear solver. Due to these challenges, it can be hard to simulate device dynamics in the time domain, which is why an accessible tool for this task can be useful.

The convolution integrals appear in a set of coupled Ordinary Differential Equations (ODEs) that represent body forces in different degrees of freedom and the volumetric flow in the device. These coupled ODEs can be represented and solved in several ways. There are nonlinear components of the ODEs, such as viscous drag and air compressibility, that make finding a solution a bit more complicated. Kurniwan's work represents the system dynamics using a bond graph, then solves the system with a software called 20sim [23]. Other people utilize Matlab Simulink's capabilities to capture some of the device dynamics. In Bailey's work, they use Proteus DS to model the mooring and wave inputs and pair it with a block diagram in Simulink to account for the effects from viscous drag [2].

Perez and Fossen have used frequency domain identification state space realization to approximate the radiation impedance FRFs associated with body motion for floating devices [32]. Additionally, Kurniawan analyzed the effectiveness of this state-space realization technique for the body motion FRFs and concluded that it adequately simulated device dynamics in the time domain, when compared to convolution integration [24]. Neither of these works considered state space realization for the FRFs associated with internal water column motion. Therefore, this work seeks to show that the convolution terms related to the internal water column motion can be approximated using state space realization.

Matlab and Simulink are powerful tools when considering marine structures. Perez and Fossen created a tool box to identify the radiation force state space realization given frequency domain hydrodynamic coefficients [32]. This toolbox prepares terms essential to time domain modeling, but does not have the capabilities to simulate the time domain response of a floating OWC WEC. Block Diagrams in Simulink are a popular way to model other WECs. WECSim is an open access software based in Simulink that can model several WEC archetypes, included fixed, but not floating, OWCs [39]. Due to the nature of the coupled ODEs and Simulink's powerful dynamic modeling capabilities, the dynamics of a floating OWC WEC should be able to be entirely modeled in MatLab and Simulink. This body of work seeks to explore this possibility and create a time domain modeling tool based in MatLab and Simulink, where the user can input the wave conditions and hydrodynamic coefficients into a script to predict the time domain response of a device.

Determining the hydrodynamic coefficients of a marine structure is not trivial, and special software is typically used to find these values. In order to find hydrodynamic coefficients, the Boundary Element Method (BEM) is often used to solve for the velocity potential on the wetted surface of the body [27]. Many regard WAMIT as a reliable tool due to the relative ease-of-use compared to several programs such as ANSYS AQWA, and the improved calculations near the free surface when compared to the open-source program, NEMOH [31]. Calculations near the free surface are especially important when analyzing an OWC due to how the water surface of the moon pool directly participates in the pneumatic power conversion. Differences in phase, magnitude, and frequency when it comes to the oscillations of the internal water surface can have significant impacts on the frequency and time domain device models. Due to the importance of the hydrodynamic coefficients and the monetary expense of the software that calculates them, this body of work originally intended to create a free hydrodynamic analysis tool, one that would extract the hydrodynamic coefficients in a similar fashion to WAMIT, that was sufficient for use in floating OWCs. However, due to technical obstacles, the focus of this work shifted to modeling devices in the time domain. Therefore, this research uses WAMIT to determine the hydrodynamic coefficients of the device.

WAMIT can capture the dynamics of the internal free surface of the OWC in three different ways: i) modeling the free surface as a light piston, effectively making the device a two body system, ii) modeling the free surface as a thin plate and specifying the heave motion of the plate as a generalized mode, or iii) solving for the pressure distribution across the internal free surface [11, 12, 35]. When the internal free surface is approximated as a plate or a piston, the hidden assumption is that the internal free surface has uniform velocity throughout. This assumption holds up when considering small scale devices, when the incoming wave length is larger than the device. However, when considering large scale devices, the internal water surface is much less likely to have uniform dynamics, thus the pressure distribution model would more accurately capture the dynamics of the internal free surface [35]. The representation of the internal water column as a piston could over or under-estimate the volumetric flow across the free surface, and the use of the pressure distribution model could help alleviate these discrepancies [30].

In constructing a mathematical model for a floating OWC, many elements are considered, such as mooring, drag, air compressibility, and damping. The specifics of all of these assumptions and consideration are discussed in Chapter 2 of this thesis, where the full mathematical model of the WEC is presented.

## 1.5 An Exploration of the BBDB's Geometry

Since hull geometry impacts performance of ships and other marine structures, it is reasonable to assume that hull and device shape will impact the conversion efficiency of a floating OWC. This assumption is supported by several studies that different researchers have conducted to explore the BBDB's geometry.

The wetted profile of the BBDB is most generally described as a rectangle. Within the constraint of a rectangular wetted surface, several researchers have explored how different geometry traits, like device length, draft, water column size, and center of gravity, can impact device performance. Suzuki et al conducted a 2-D profile numerical optimization study with different turbines that revealed how different lengths, drafts, and turbine sizes affected efficiency [41]. This study did not aim to maximize power output with changes in geometry, but to minimize device size while keeping power output constant. In order to achieve this, Suzuki determined that a device length to water column width ratio should be around 2 [41]. Other geometry characteristics can impact performance, such as the location of the center of gravity, which has less of an impact than the length of the water column duct [36]. Another study took a more detail oriented approach to geometry exploration and considered hundreds of geometries in the frequency domain, varying them parametrically using defined device characteristics [33]. This study found that forward bent duct buoys might be more efficient than BBDBs [33]. While this study was incredibly thorough when considering geometry characteristics, it is limited by the fact that it only considered performance in the frequency domain. Frequency domain analysis is a useful tool, but as discussed in the previous section, it does not capture all of the relevant device dynamics. Understanding how certain geometry characteristics impact performance without changing the general rectangular shape of the BBDB is useful, as it indicates what aspects of device design could be particularly important.

Other researchers have conducted physical tests to explore the BBDB geometry. Toyota et al considered 5 different BBDB geometries in a test wave basin. These 5 geometries were different in duct length and buoyancy chamber shape, and the researchers found that the geometries with a longer duct length performed better [42]. Wave tank tests coupled with 2D numerical tests have revealed other salient geometry traits, such as stern geometry and head-on duct profile [22]. Exploring BBDB geometry with physical experiments provides unique insights that may not be as well captured with numerical modeling. However, wave tank tests have their own limitations, such as the number of geometries able to be considered in a reasonable length of time.

The BBDB geometry is challenging to optimize due to how the modes of motion are coupled. Three main modes of motion are important for power generation in a BBDB: surge, heave, and pitch [36]. These directions and their definitions are presented in Figure 1.3. While trying to tune one mode of motion, the others are likely to be impacted and affect performance, and there is no way of predicting this impact without numerical or physical tests. Utilizing multiple degrees of freedom increases the range of frequencies that can be captured by this device and can lead to better power generation in real wave conditions, which can help lower the levelized cost of energy. One of the goals of this body of work is to explore different geometry traits of the BBDB, including non-rectangular wetted profiles, and see how changes in geometry affect performance in a 3D time domain simulation.

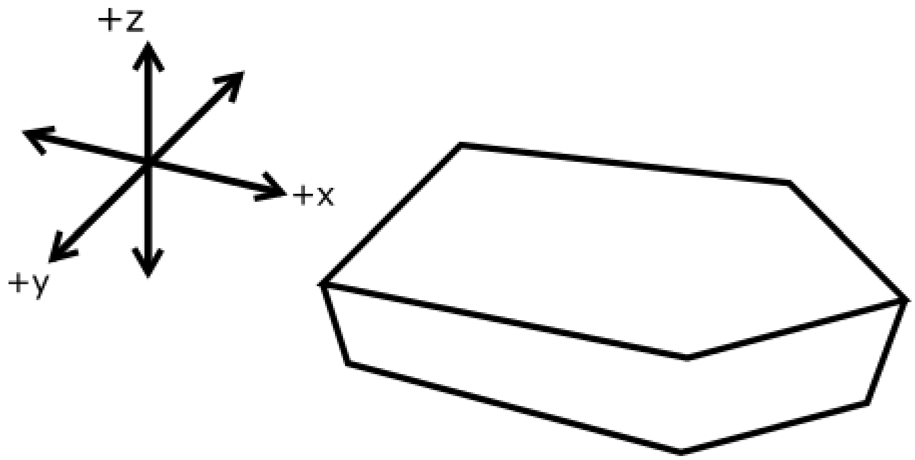

Figure 1.3: Demonstration of body motion directions for a marine structure. Heave is in the z direction, surge is in the x direction, sway is in the y direction, roll is rotation about the x axis, pitch is rotation about the y axis, and yaw is rotation about the z axis.

## 1.6 Research Outline

This thesis will explain the numerical modeling techniques and code associated with a time domain modeling tool for floating OWCs, and then demonstrate that tool's use by exploring BBDB hull geometry. Chapter 2 will shed light on potential flow theory and the mathematical model. The mathematical model includes considerations for mooring, viscous drag, and air compressibility. Chapter 3 will explain the development of a time domain simulation tool for a floating OWC. The time domain simulation tool consists of a MatLab script that determines the FRFs and their state space representation, and then a block diagram in SimuLink that solves the nonlinear system of ODEs. This chapter will compare the state space representation to convolution integration. Chapter 4 will validate the time domain simulation tool by comparing simulated results with known experimental results. Finally, Chapter 5 will demonstrate the time domain modeling tool. The demonstration will explore the BBDB geometry and how the shape of the wetted surface can impact performance.

# Chapter 2

# Background of the Mathematical Model of an OWC WEC

This chapter reviews some basic hydrodynamic theory, then explains the essential governing equations, assumptions, and relevant literature before presenting a final mathematical model.

## 2.1 Hydrodynamic Theory

This body of work considers water to be an ideal fluid, which assumes that water is incompressible (has a constant density), that its flow is inviscid (frictionless) and irrotational, and that mass and energy are conserved [26]. A vector ($\vec{v}$) describes the velocity of a fluid particle. The mass conservation property can be described by

$$\nabla \cdot \vec{v} = 0, \tag{2.1}$$

while irrotational flow is represented by

$$\nabla \times \vec{v} = 0. \tag{2.2}$$

These conditions allow for

$$\vec{v} = \nabla\phi \tag{2.3}$$

to define the velocity potential ($\phi$) [13]. The velocity potential contains information about the fluid, is the basis of linear potential flow theory, and is what some software, such as WAMIT, solves for when considering marine structures.

Figure 2.1 shows the coordinate system used in this body of work, where the average free surface lies on the z=0 plane and the y axis goes into the page. One can define the free surface of the wave to be $F(x, y, z, t) = z - \eta(x, y, t) = 0$ [34]. When $z = \eta$, the fluid pressure is equal to the air pressure on the surface of the water [34].

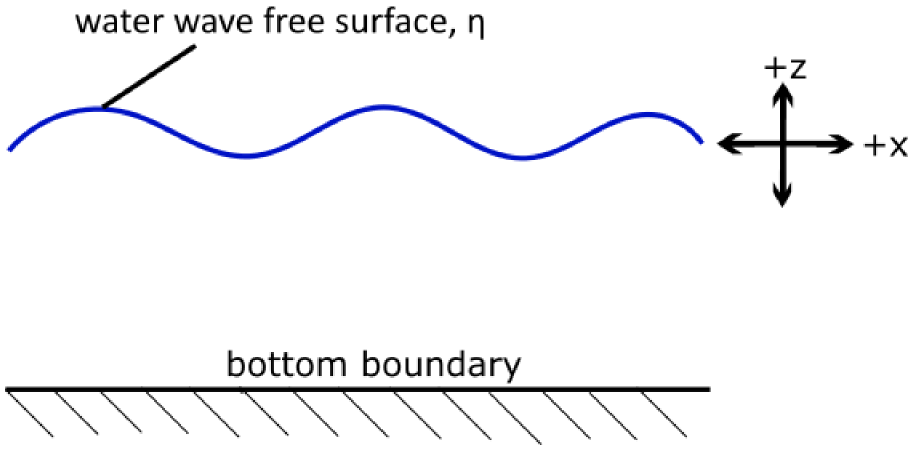

Figure 2.1: A representation of a water wave and a depiction of the coordinate system used in this work.

When considering a three dimensional partially submerged structure, six degrees of freedom apply:$(x, y, z, \omega_x, \omega_y, \omega_z)$, or, surge, sway, heave, roll, pitch, and yaw. The positive $x$ axis is generally assumed to be in the propagation direction of an incident wave. When there is a floating structure, not only does the incident wave act on the body, but the motions of the body affect the surrounding water. When the motions of the body produce waves, those waves are known as radiated waves [13]. These radiated waves appear in the velocity potential of the fluid, which can be represented by

$$\varphi = \varphi_R + \varphi_D, \tag{2.4}$$

where $\varphi_R$ represents the radiation potential and $\varphi_D$ represents the diffraction potential [43]. The radiation potential comes from the radiated waves and is equivalent to

$$\varphi_R = i\omega \sum_{j=1}^{7} \xi_j \varphi_j, \tag{2.5}$$

where $\omega$ is frequency in rad/s, $\xi_j$ is the body motion in the $j^{th}$ direction, and $\varphi_j$ is the radiation potential in the $j^{th}$ direction [43]. The diffraction potential can be represented by

$$\varphi_D = \varphi_0 + \varphi_S, \tag{2.6}$$

where $\varphi_0$ is the velocity potential from the incident wave and $\varphi_S$ is the velocity potential caused by a scattered disturbance, which occurs when the incident wave runs into a body [43].

The radiation and diffraction potentials are important when considering floating OWCs, since these potentials are the basis of the FRFs used to predict the motions of the body and the internal water surface. These FRFs and the equations that use them are explained in the following section.

## 2.2 Basic Governing Equations

Two equations capture the basic dynamics of a floating OWC in the frequency domain. The first equation,

$$Q_w = qA - Yp - \sum_j H_j^u u_j, \quad j = 1, \ldots, 6, \tag{2.7}$$

represents the volume flow of water through the internal free surface of the moon pool ($Q_w$) [13]. The unknowns of this equation are the air chamber pressure inside the device ($p$) and the body velocities in each direction ($u_j$). The amplitude of the incident wave ($A$) is multiplied by the excitation volume flow ($q$). The excitation volume flow is the volume flow across the internal free surface that is caused by the wave input. The radiation admittance FRF ($Y$) accounts for the volume flow associated with the applied pressure on the internal surface. The Radiation Coupling FRFs ($H_j^u$) accounts for the volume flow caused by body motions in each direction. The Radiation Coupling FRFs also link the equation for $Q_w$ and the equations for the forces acting on the body.

The force acting on the body in each degree of freedom can be calculated by

$$F_j = f_j A - \sum_{j'} Z_{jj'} u_{j'} - H_j^p p, \quad j = 1, \ldots, 6, \tag{2.8}$$

where $F_j$ is the total force acting on the body in the $j^{th}$ direction [13]. The unknowns, $p$ and $u_j$, are the same as in Equation 2.7. The excitation force FRF ($f_j$) is the body force caused by the wave inputs. The radiation impedance FRFs ($Z_{jj'}$) account for forces caused by the radiation damping and the added mass coefficients. $H_j^p$ is equivalent to $-H_j^u$ from Equation 2.7 [13].

These frequency domain equations capture the basic dynamics of a floating OWC subjected to an incident wave. Cummins discovered that when he turned the individual FRFs in the two above equations into IRFs using a Fourier Transform, he could use the IRFs in convolution integrals to model the time domain response [6]. Applying Cummins's technique to Equations 2.7 and 2.8 results in the basic time domain equations that govern the dynamics of a floating

OWC. The volume flow through the internal free surface and the body force in each degree of freedom is calculated by

$$\begin{aligned} Q_w(t) = &\int_{-\infty}^{\infty} q(t-\tau)A(\tau)\mathrm{d}\tau - \int_{-\infty}^{t} y(t-\tau)p(\tau)\mathrm{d}\tau \\ &- \sum_j \left[ C_j(\infty)u_j + \int_{-\infty}^{t} h_j^u(t-\tau)u_j(\tau)\mathrm{d}\tau \right], \end{aligned} \tag{2.9}$$

$$\begin{aligned} F_j(t) = &\int_{-\infty}^{\infty} f_j(t-\tau)A(\tau)\mathrm{d}\tau \\ &- \sum_{j'} \left[ a_{jj'}(\infty)\dot{u}_{j'} + \int_{-\infty}^{t} z_{jj'}(t-\tau)u_{j'}(\tau)\mathrm{d}\tau \right] \quad , \\ &+ C_j(\infty)p + \int_{-\infty}^{t} h_j^u(t-\tau)p(\tau)\mathrm{d}\tau, \quad j = 1, \ldots, 6 \end{aligned} \tag{2.10}$$

where $C_j(\infty)$ are infinite radiation coupling coefficients and $a_{jj'}(\infty)$ are the infinite added mass coefficients [23]. Equations 2.10 and 2.9 are the basis of a more complex mathematical model that considers things such as air compressibility, viscous drag, turbine loading, and mooring forces. Fortunately, the basis of this model is linear potential flow theory, allowing for the advantage of the superposition principle. Approximations and models that account for other physical effects can be simply added to or subtracted from Equations 2.10 and 2.9.

There are many different mathematical models and techniques that can be used to account for the physics of these real systems, and the following sections in this chapter will explain each model and the justification for its use.

## 2.3 Viscous Drag

Drag is a force caused by fluid friction and viscous drag affects the body motion of a floating structure. Bull considers viscous drag from the drag force portion of the Morison Equation,

$$F_{D,j} = \frac{1}{2}\rho A C_{D,j}(u_j - v_j)|u_j - v_j|, \tag{2.11}$$

where $\rho$ is the density of water, $C_D$ is the drag coefficient, $A$ is the surface area of the body that is perpendicular to the fluid velocity, and $v_j$ is the velocity of water in the $j^{th}$ direction [3]. In Bull's work, she discretizes the body of the WEC and calculates the drag for discretized section. This thesis takes a lower fidelity approach. The fluid velocity near the body is approximated by estimating the fluid velocity of the incident wave at that point in time and from the velocity of the internal water column. The fluid velocity of the incident wave is estimated using the Airy wave theory. The Airy wave theory gives the vertical and horizontal particle velocity, respectively, by

$$v_3 = \frac{\pi H}{T}\frac{\sinh[k(z+d)]}{\sinh(kd)}\sin\theta, \tag{2.12}$$

$$v_1 = \frac{\pi H}{T}\frac{\cosh[k(z+d)]}{\sinh(kd)}\cos\theta, \tag{2.13}$$

where $H$ is the wave height, $T$ is the wave period, $k$ is the wave number, $z$ is the distance from the mean surface, $d$ is the average water depth, and $\theta = kx - \omega t$, where $x$ is the propagation distance, $\omega$ is the wave frequency, and $t$ is time [10].

The drag coefficient can be approximated by comparing geometries to shapes with known drag coefficients, such as Bailey did when they estimated the drag coefficient based on experimental results for a structure subjected to oscillating flow [2].

## 2.4 Mooring

The mooring system of a WEC attaches the WEC to the bottom of the ocean and determines how the device maintains its position in the water [20]. Mooring interacts intimately with body motion, simultaneously contributing restoring and damping forces to the system [20]. The kind of mooring and how it is approximated in the model can significantly affect the dynamic response of a WEC, thus selecting an adequate technique is critical [2]. For floating OWCs, many use a softer mooring system, such as the slack lined catenary system shown in Figure 2.2, but this is not necessarily the best decision, since in certain wave conditions, a stiffer mooring system can increase power generation [36].

Mooring models can be incredibly complex, especially when lines are taught, since taught lines introduce significant nonlinear effects [20]. The most complex mooring models involve conducting finite element analysis on each mooring line in order to accurately describe the impact of the wave excitation on the mooring line, how the line interacts with the sea floor, and how the motion of the line affects the motion of the WEC, among other considerations [7]. The most simplistic mooring models involve linearizing the stiffness and damping of the mooring lines and determining the applied forces by multiplying these linear coefficients by the body velocity or displacement [7].

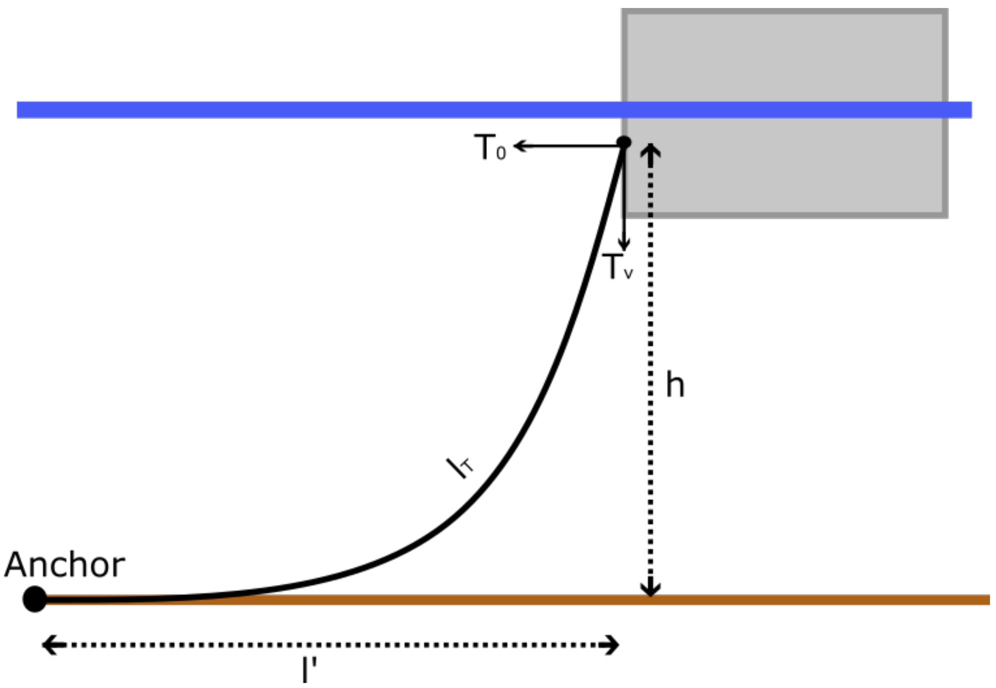

Figure 2.2: An example of a slack catenary mooring line attached to a floating structure with the variables used in the mathematical model represented.

This body of work considers a catenary mooring model, demonstrated in Figure 2.2. This model, derived by Garza-Rios et al, calculates the horizontal and vertical tension on the mooring line where it is attached to the floating body [14]. As the device moves, the model determines a new line tension that acts as a static restoring force on the structure. The model is based on catenary line equations that approximate the basic geometry of a catenary line. While the model does not consider how the general shape of a mooring line may change due to external forces, it does consider the material, dimensions, and initial conditions of the mooring line [14]. One can directly determine the horizontal and vertical tension components, $T_0$ and $T_v$, respectively, by

$$\sinh\left(\alpha\left(\sqrt{h\left(h+\frac{2}{\alpha}\right)}+\ell'-\ell_T\right)\right)-\alpha\sqrt{h\left(h+\frac{2}{\alpha}\right)}=0 \tag{2.14}$$

$$\alpha = \frac{P}{T_0} \tag{2.15}$$

$$T_v = P\sqrt{h\left(h + 2\frac{T_0}{P}\right)}, \tag{2.16}$$

where $P$ is the line weight per unit length, $h$ is the vertical displacement between the anchor and the connection point on the body, $l'$ is the horizontal distance between the anchor and the connection point on the body, and $l_T$ is the total length of the mooring line [14].

Mooring lines provide not only restoring forces, but also damping forces. It can be challenging to anticipate the damping coefficients of a catenary line, since the damping effects come from hydrodynamic drag, interaction with the sea floor, and internal friction within the chain [21]. This body of work considers a small amount of damping due to mooring lines. The damping coefficients are found through tuning models to an experimental result or by using estimated damping values from literature, depending on the observed WEC.

This mooring model is two-dimensional, while the model of the WEC is three-dimensional. In order to satisfy the discrepancies between these different models, one can assume that certain directions in the mooring model correlate with certain directions in the WEC model. This work assumes that the vertical tension applies force solely in the heave ($z$) direction. The horizontal tension applies force in the surge ($x$) and sway ($y$) directions. One can estimate the force applied in the surge and sway directions from $T_0$ by using trigonometric relations and the angle that the line makes with the body's coordinate system at equilibrium. If multiple mooring lines act on the body, one can sum the force in each direction. The mooring restoring force ($F_M$) in the mathematical model for the WEC can be represented by

$$\begin{aligned} F_M &= T_{0,j}, \quad j = 1, 2, \\ F_M &= T_v, \quad j = 3, \end{aligned} \tag{2.17}$$

where $T_{0,j}$ is the horizontal tension component in the j direction. The mooring damping force $F_MD$ is represented by

$$F_{MD,j} = C_{M,j} u_j, \quad j = 1, 2, 3, \tag{2.18}$$

where $C_{M,j}$ is the mooring damping coefficient and j represents the degree of freedom.

## 2.5 Air Compressibility and Turbine Dynamics

Since the PTO of the WEC relies on the pressure differential between the internal air chamber of the WEC and the atmosphere, air compressibility can impact power generation estimates. This model from Sheng assumes that air is isentropic and considers different equations based on if air is going into or out of the chamber [38]. The volume flow across the turbine, $Q_p$, when the gauge pressure inside the chamber is greater than zero, causing air to leave the chamber, is

$$Q_p = \frac{dV}{dt} - \frac{V}{\gamma p_0 + p} \frac{dp}{dt}, \tag{2.19}$$

where $Q_w = \frac{dV}{dt}$ represents the volume flow across the internal water surface, $p$ is the gauge pressure inside the chamber, $\gamma$ is air's specific heat ratio (usually 1.4), and $V$ is the volume of air inside the chamber [38]. When the gauge pressure inside the chamber is negative, causing air to enter the chamber,

$$Q_p = \left(1 + \frac{p}{\gamma p_0}\right) \frac{dV}{dt} - \frac{V}{\gamma p_0} \frac{dp}{dt}. \tag{2.20}$$

These equations have two unknowns: the gauge pressure in the chamber, $p$, and the volume flow across the PTO, $Q_p$. Here is where turbine dynamics fill in the gaps. For a linear turbine, like the Wells Turbine, the relation between $p$ and $Q_p$ is

$$Q_p = \frac{p}{k_1}, \tag{2.21}$$

where $k_1$ is the air flow damping coefficient [38]. With this relation, only $p$ remains as an unknown. This is convenient, since Equations 2.9 2.10 and 2.10, the foundation of the mathematical model, also have $p$ as an unknown.

Finding the instantaneous power output from the turbine model is straightforward and can be represented by

$$P_{instant} = p(t)Q_p(t), \tag{2.22}$$

where $P_{instant}$ is pneumatic power [13]. This relation does not consider inefficiencies from the electrical generator or from the turbine. This body of work is concerned with the pneumatic efficiency of the device, thus only pneumatic power is calculated.

## 2.6 Restoring Forces

Floating marine structures experience hydrostatic restoring forces, such as gravitational and buoyancy forces, in different degrees of freedom. Hydrostatic force coefficients, $S_{i,j}$, are one of the outputs that WAMIT provides. The hydrostatic force can be found by taking

$$F_{hs,i} = S_{i,j}s_j, \tag{2.23}$$

where $F_{hs,i}$ is the force in the $i^{th}$ direction and $s_j$ is the body displacement in the $j^{th}$ direction.

## 2.7 Final Equations for Time Domain Simulation

With the model considerations explained in this chapter, the full mathematical model is more easily understood.

One can find the total volume flow across the free surface and across the turbine by first considering the volume flows caused by the incident wave, the pressure on the internal free surface, and velocity of the body. The displacement of the body also contributes its own volume displacement. The volume flow across the free surface directly relates to the volume across the turbine. The relation is clearly outlined in Section 2.5, and results in $Q_p$, the volumetric flow across the turbine. The volume flow across the internal free surface ($Q_w$), and therefore the volume flow across the turbine ($Q_p$), can be calculated by

$$\begin{aligned}
&Q_w(t) = q * A(t) - y * p - \sum_j \left[C_j(\infty)u_j + h_j^u * u_j\right] - r_j u_j, \\
&Q_w = \frac{Q_p + \frac{V}{\gamma p_0}\frac{dp}{dt}}{\left(1 + \frac{p}{\gamma p_0}\right)}, && p < 0 \\
&Q_w = Q_p + \frac{V}{\gamma p_0 + p}\frac{dp}{dt}, && p > 0 \\
&Q_p = \frac{p}{k_1}, \\
&p(0) = 0,
\end{aligned} \tag{2.24}$$

where $r_j$ is a transformation factor based on the WEC geometry and the degree of freedom, and $*$ indicates the convolution integral [23]. When $j = 3$, $r = A_i$, where $A_i$ is the internal surface area. When $j = 5$, $r = -x_b A_i$, where $x_b$ is the distance in the $x$ direction between the center of the internal free surface and the center of buoyancy of the body [23].

In order to calculate the total force on the body in each direction, several sources of force need to be considered, since they will contribute to the total force acting on the body.

There is a force caused by the incident wave amplitude, known as the excitation force. The added mass and radiation damping, the pressure in the internal chamber, the mooring, and additional hydrostatic effects also contribute to the total force. The total force on the body in each degree of freedom is equivalent to $m_m \ddot{u}_j(t)$, where $m_m$ is the device mass and $\ddot{u}_j(t)$ is the acceleration of the body. The acceleration of the body in each degree of freedom can be calculated by

$$\begin{aligned} m_m \ddot{u}_j(t) = f_j * A(t) - \sum_{j'} &\left[ a_{jj'}(\infty) \dot{u}_{j'} + z_{jj'} * u_{j'} \right] \\ &- \left[ C_j(\infty) p + h_j^u * p \right] - F_{M,j} - F_{MD,j} - F_{D,j} - r_j p - F_{hs}, \quad j = 1, \ldots, 6, \\ &s_j(0) = 0, \\ &u_j(0) = 0, \end{aligned} \tag{2.25}$$

where $r$ is the same transformation factor used in Equation 2.24 [23]. When solving the system of equations, there are as many force equations as there are body motion directions. All initial conditions are zero.

This body of works solves Equations 2.24 and 2.25 using a block diagram in SimuLink, which is the basis of the time domain modeling tool created in this work. The techniques used to find pertinent functions and coefficients are described in the next section. This next section also explains the methods used to solve these equations.

# Chapter 3

# Methodology of Device Simulation in the Frequency and Time Domain

The mathematical model from the previous chapter captures the physical effects acting on a floating OWC. To adequately predict the WEC time domain response, it is essential to use appropriate modeling tools to evaluate this model. This chapter will explain the numerical techniques used to evaluate this model and describe the implementation of these techniques that create the time domain modeling tool.

The modeling tool described in this chapter is known as the Floating Oscillating Water Column Iterative Time Series Solver (FlOWCITSS, pronounced flow-kits). FlOWCITSS is intended to be used to evaluate any floating OWC in multiple degrees of freedom. FlOWCITSS is open access and shared in a github repository, noted in Appendix A.

The general work-flow for FlOWCITSS is shown in Figure 3.1. Before FlOWCITSS can be used, one must first model the WEC's geometry and determine the hydrodynamic and hydrostatic coefficients of the device using WAMIT. The user can then import these coefficients into MatLab, where FlOWCITSS can use them to evaluate device performance. FlOWCITSS does this by first generating the FRFs, IRFs, and state space representations that are relevant to the mathematical model. Then, a block diagram in Simulink references the variables in the MatLab work space and steps through time to numerically calculate the unknowns. At each time step, FlOWCITSS outputs the device motion, chamber pressure, and instantaneous pneumatic power from the floating OWC.

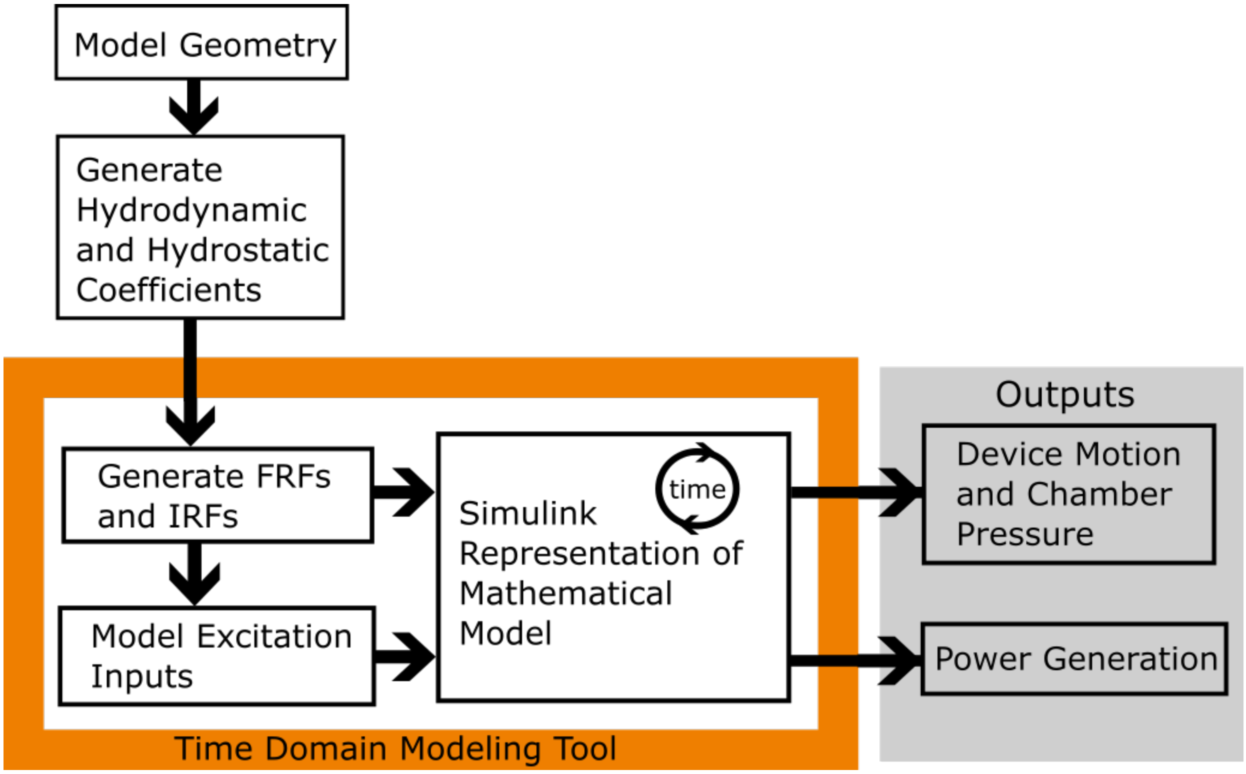

Figure 3.1: A diagram explaining the simulation process and where in the process the modeling tool operates.

## 3.1 Inputs to the Modeling Tool

FlOWCITSS accepts hydrodynamic and hydrostatic coefficients from WAMIT. The required WAMIT outputs are the excitation force, radiation damping, added mass, and hydrostatic coefficients. In WAMIT, the user determines the range of evaluated frequencies based on each geometry. The excitation force and volume flow FRFs go to zero as $\omega \to \infty$, and WAMIT needs to evaluate the frequency range that encompasses the FRF prior to and during this decay in order to accurately assess the time domain performance of a device.

To capture the dynamics of the internal water column, in WAMIT the user should distribute the field points across the internal free surface and output the vertical velocity at each field point. An example of distributed points is shown in Figure 3.2, where white boxes represent the distributed points on the free surface. This allows FlOWCITSS to use the pressure distribution method, which the next section explains further.

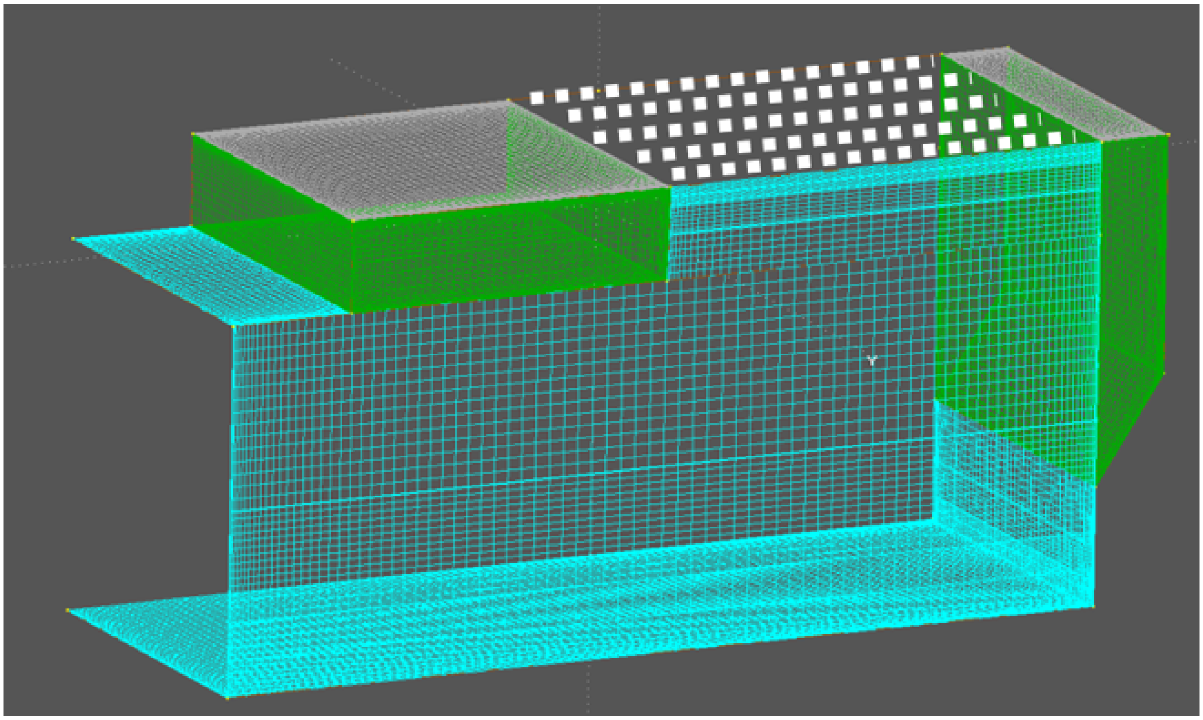

Figure 3.2: A depiction of field points distributed across the internal free surface of a body.

In FlOWCITSS, the user will also specify the frequency range and step size, the wave heading range and step size, the discretization of the field points, the mass of the device, the device's characteristic length, the density of sea water, the directions of the body's motion (such as heave, surge, and pitch), the area of the internal free surface, drag coefficients, incident wave data, mooring characteristics, and turbine characteristics.

## 3.2 Frequency Domain

WAMIT outputs nondimensional frequency domain data for marine structures. FlOWCITSS dimensionalizes WAMIT's outputs according to WAMIT's manual and turns them into FRFs [43].

The pressure distribution model is a way of capturing the internal water column dynamics of a floating OWC. This model requires three different FRFs: excitation volume flow, radiation admittance, and radiation coupling.

The excitation volume flow FRF is theoretically defined by

$$q = \frac{1}{A} \iint_S \frac{\partial \phi_D}{\partial z} dS, \tag{3.1}$$

where $A$ is the incident wave amplitude, $S$ indicates the internal surface of the water column, and $\frac{\partial \phi_D}{\partial z}$ is the diffracted velocity potential differentiated in the $z$ direction, which is equivalent to the diffracted water velocity on the free surface [23]. To calculate this FRF from the WAMIT outputs, FlOWCITSS numerically integrates the diffracted portion of the water velocity across the distributed field points on the free surface for every frequency and every wave heading. From $q$, FlOWCITSS calculates the radiation admittance FRF, $Y$, by using reciprocity relations [13]. The radiation admittance is represented by

$$Y = G + iB, \tag{3.2}$$

where the real part, $G$, is the radiation conductance and the imaginary part, $B$, is the radiation susceptance [13]. The reciprocity relation relating $G$ to $q$ is

$$G = \frac{k}{4\pi\rho g v_g} \int_0^{\pi} |q(\beta)|^2 \mathrm{d}\beta, \tag{3.3}$$

where $v_g$ is the group velocity of the incoming wave, $\beta$ is the incident wave heading, $\rho$ is the density of water, $k$ is the wave number of the incident wave, and $g$ is the acceleration due to gravity [13]. The radiation conductance FRF directly relates to the radiation susceptance FRF by

$$B(\omega) = -\frac{2\omega}{\pi}\int_0^\infty \frac{G(y)}{\omega^2 - y^2}\mathrm{d}y, \tag{3.4}$$

where $\omega$ is the frequency of $B$ and $y$ is the frequency of $G$ [13]. FlOWCITSS calculates $B(\omega)$ with techniques used to evaluate Kramers-Kronig transformations [29]. FlOWCITSS interpolates $G$ in the frequency domain to a significantly more refined sample size. Then, for each frequency, FlOWCITSS integrates the term in Equation 3.4 for all frequencies except the one being evaluated, omitting the singularity where zero would appear in the denominator.

The excitation volume flow and the radiation admittance FRFs represent the effects of the incident wave and the chamber pressure on volume flow. One final group of FRFs remains in the pressure distribution model: the radiation coupling terms that relate body motion to volume flow across the free surface and chamber pressure to body force. The radiation coupling term is calculated by

$$H_j^u = -\iint_S \frac{\partial \varphi_j}{\partial z} dS = C + iJ, \tag{3.5}$$

where $C$ is the real part, $J$ is the imaginary part, $j$ is the body motion direction, and $\frac{\partial \varphi_j}{\partial z}$ is the radiated portion of the velocity potential differentiated in the $z$ direction, which is equivalent to the radiated part of the water velocity on the free surface [13]. FlOWCITSS calculates $H_j^u$ similarly to $q$, by integrating the water velocity across the internal free surface for each body motion direction and frequency. $H_j^u$ relates body velocity to volume flow, while $H_j^p$ relates chamber pressure to body force. These two terms are related by $H_j^u = -H_j^p$.

The remaining FRFs of interest are the excitation force FRFs and the radiation impedance

FRFs. These are significantly simpler to evaluate, since WAMIT outputs them directly. FlOWCITSS dimensionalizes the terms and organizes them based on degree of freedom and frequency. The excitation force FRF is determined by summing the real and imaginary components of the excitation force outputs from WAMIT [43]. The radiation impedance FRFs exist for all body motion directions and are determined from the added mass and radiation damping coefficient outputs from WAMIT [43].

## 3.3 Time Domain

### 3.3.1 Excitation Inputs

The excitation inputs to the mathematical model solely depend on the incident wave, which is known at each time step. This makes it straightforward to evaluate the excitation inputs prior to entering the block diagram. To calculate these inputs, FlOWCITSS evaluates the IRFs of the excitation inputs, then convolves them with the incident wave elevation in the time domain. The body force and volume flow excitation inputs have both real and imaginary parts. FlOWCITSS uses both parts to determine the IRFs by calculating

$$X_i(t) = \frac{1}{\pi}\int_0^\infty \left[\mathrm{Re}\left(X_i\right)\cos\omega t - \mathrm{Im}\left(X_i\right)\sin\omega t\right] d\omega, \tag{3.6}$$

where $X_i(t)$ denotes either the volume flow or body force excitation IRF and $X_i$ represents the FRF of the excitation input being evaluated [43]. The integral in Equation 3.6 goes from zero to infinity, but in practice, both the excitation volume flow and the excitation force decay to zero as $\omega \to \infty$, thus FlOWCITSS evaluates the range of frequencies that have not yet sufficiently decayed.

To determine the excitation inputs in the time domain, the modeling tool convolves the IRF and the incident wave by

$$E(t) = \int_{-\infty}^{\infty} X_i(t-\tau)A(\tau)\mathrm{d}\tau, \tag{3.7}$$

where $E(t)$ is the excitation input, $\tau$ is a time integration variable, $X_i(t-\tau)$ represents the IRF, and $A(\tau)$ is the user defined incident wave elevation. FlOWCITSS defines both the incident wave and the IRF for a user defined time range and time step, then convolves these two time series by applying the convolve MatLab function to the data in the time series. Next, FlOWCITSS multiplies the resulting vector by the size of the time step and truncates it so it is the same length as the original time series. This technique essentially numerically solves the convolution integral with the Euler method. This numerical technique has been bench-marked against analytical convolution integration and is found to match the analytical solution for a sufficiently small time step.

### 3.3.2 Convolution Integration and State Space Representation

Numerical integration is well suited to calculate the convolution terms in the mathematical model that can be evaluated outside of the time step iteration process, such as the excitation inputs. However, numerical convolution integration becomes challenging inside the block diagram due to how SimuLink processes signals. Numerical integration of a convolution term requires a complete time history of the response. When this complete time history has to be accessed at every time step, the process becomes cumbersome in SimuLink. Circumventing these issues is relatively straightforward: use a state space representation to approximate the dynamic response in the time domain.

Previous works have shown that a frequency domain identification state space realization is adequate for the radiation impedance terms (radiation damping and added mass) [24, 32].

However, the same cannot be said for the radiation coupling and radiation admittance terms that arise from the pressure distribution model. This body of work seeks to demonstrate that a state space realization of the radiation coupling and radiation admittance terms is sufficient to approximate the convolution integral, and therefore sufficient to model floating OWCs in the time domain.

The state space realization technique used in this body of work is FRVF (Fast Relaxed Vector Fitting). Gustavsen created a MatLab function, vecfit3, that uses FRVF to take tabulated frequency domain data and generate a rational function approximation [9, 15, 16]. FlOWCITSS uses FRVF because it is robust and straightforward to use. FlOWCITSS in intended to evaluate many different kinds of floating OWCs. Since FRFs change depending on the device geometry, using a robust and flexible state space realization tool will help ensure the adequacy of this tool for a wide range of geometries.

In order to show that a state space realization approximation is sufficient for the radiation coupling and radiation admittance terms, the modeling tool will process the frequency domain WAMIT outputs for RM6, the generic BBDB archetype created by Sandia National Labs. The radiation admittance FRF is shown in Figure 3.3, while the heave and pitch radiation coupling FRFs are shown in Figures 3.4 and 3.5, respectively.

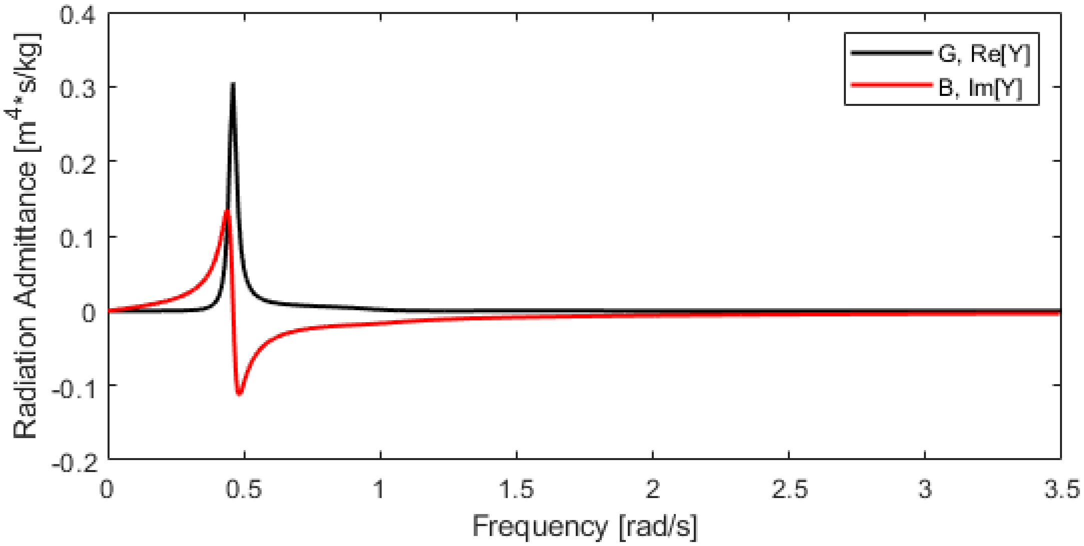

Figure 3.3: Radiation Admittance FRF ($Y$) for RM6

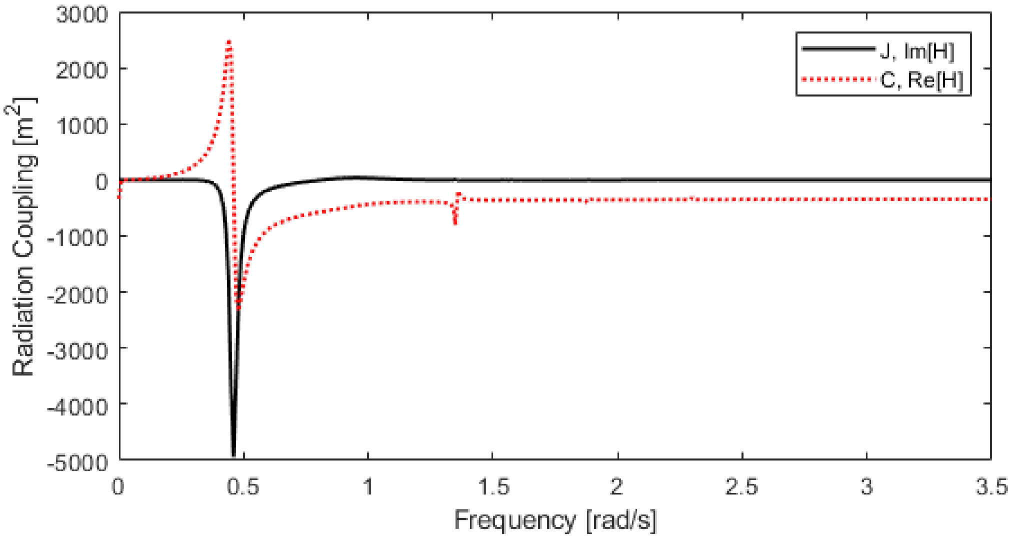

Figure 3.4: Radiation Coupling Heave Term FRF ($H_3^u$) for RM6

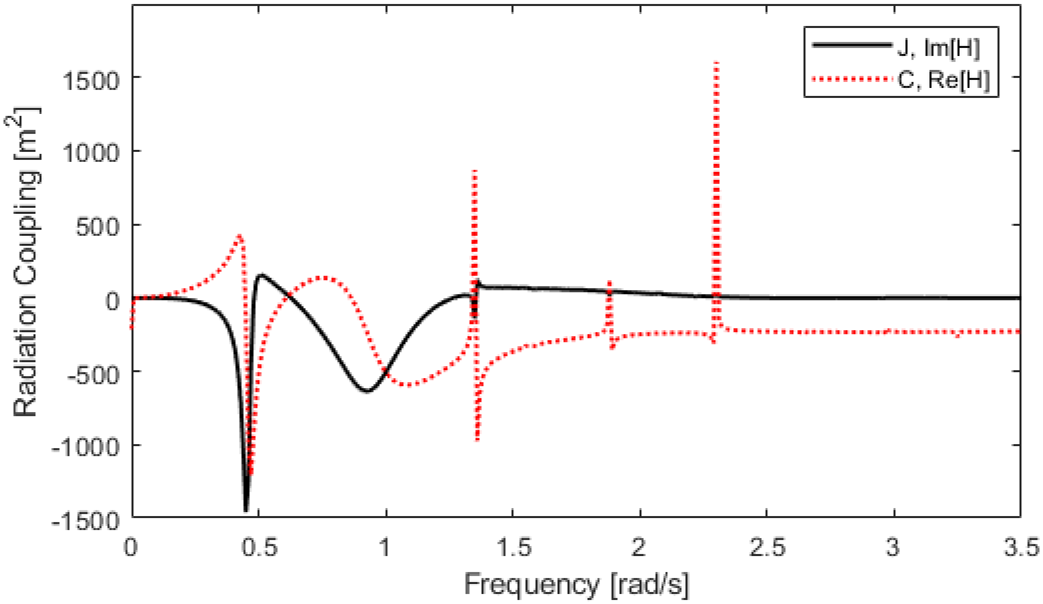

Figure 3.5: Radiation Coupling Pitch Term FRF ($H_5^u$) for RM6

FlOWCITSS inputs these FRFs into vecfit3 using slightly different conventions. The radiation coupling term in Equations 2.24 and 2.25 is accompanied by the real component of the radiation coupling term at infinite frequency. To compensate for this in the state space representation, the FRF for the radiation coupling term takes on the form: $H_i^u = [C - C(\infty)] + iJ$.

To compare the numerical convolution integration to the state space realization, one can evaluate the time domain response of each form due to an arbitrary sinusoidal input. The time domain response of the radiation admittance term is shown in Figure 3.6.

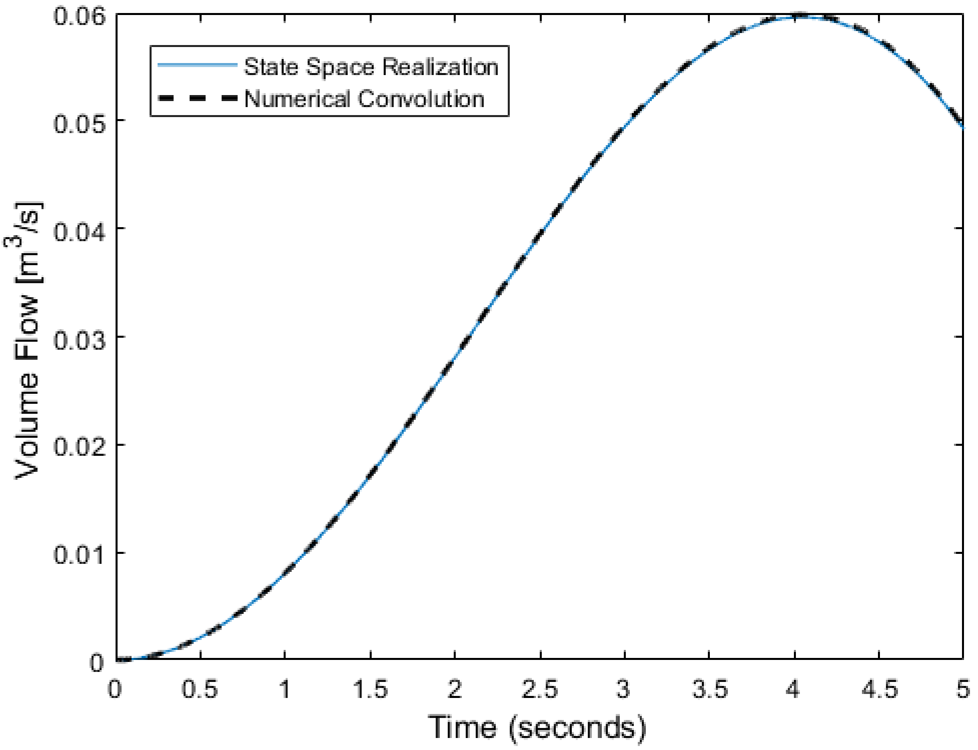

Figure 3.6: Vector Fitting and Numerical Convolution integration comparison for the Radiation Admittance term, using an arbitrary sinusoidal input

The difference between the vector fit response created using vecfit3 and the numerical convolution response is nearly indiscernible. This suggests that this state space realization approach adequately circumvents numerical convolution integration for the radiation admittance term. A similar conclusion is reached for the radiation coupling term in the heave direction, shown in Figure 3.7.

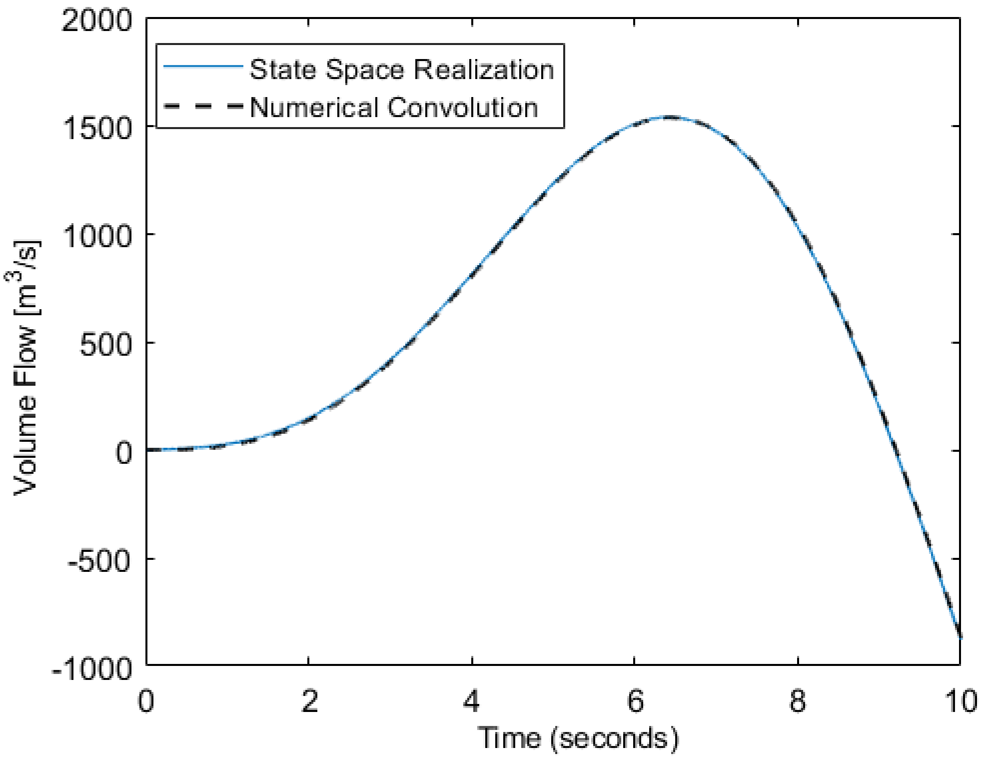

Figure 3.7: Vector Fitting and Numerical Convolution integration comparison for the Radiation Coupling Heave term, using an arbitrary sinusoidal input

The two time domain responses are practically the same. This again suggests that state space realization is a promising way to circumvent the struggles with convolution integration for the radiation coupling terms. What about when vector fitting is applied to a FRF that has more variation and is more complex than the heave radiation coupling term? The shape of the pitch radiation coupling term, shown in Figure 3.5, has more variation than the heave term. The time domain response of the pitch radiation coupling term is shown in Figure 3.8. The fit of the state space representation compared to the FRF is shown in Figure 3.9

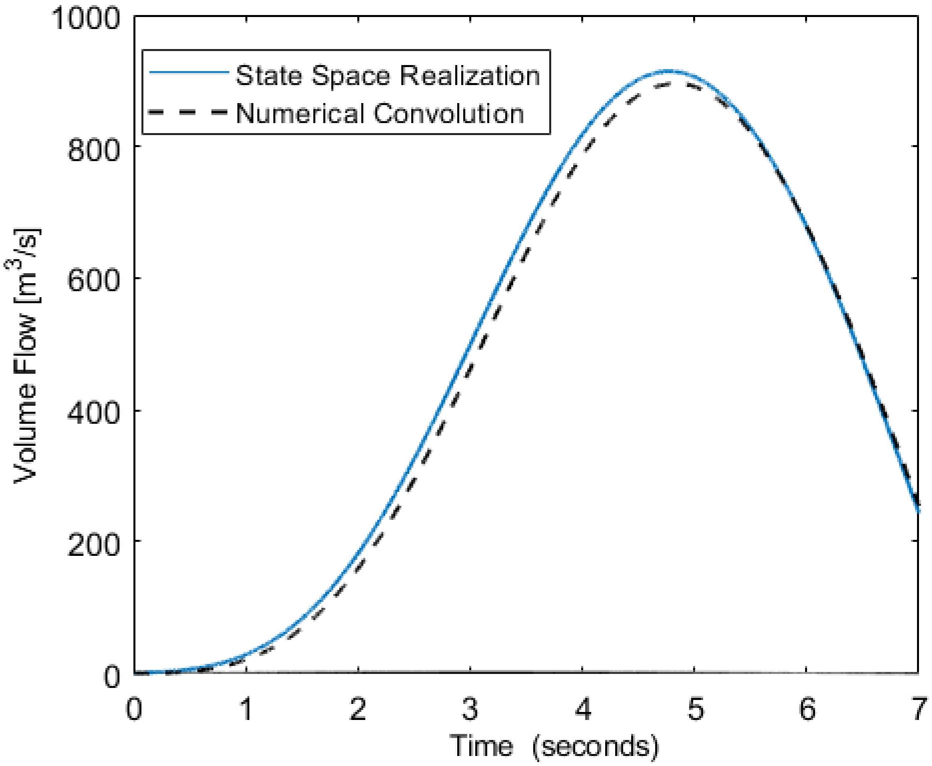

Figure 3.8: Vector Fitting and Numerical Convolution integration comparison for the Radiation Coupling Pitch term, using an arbitrary sinusoidal input

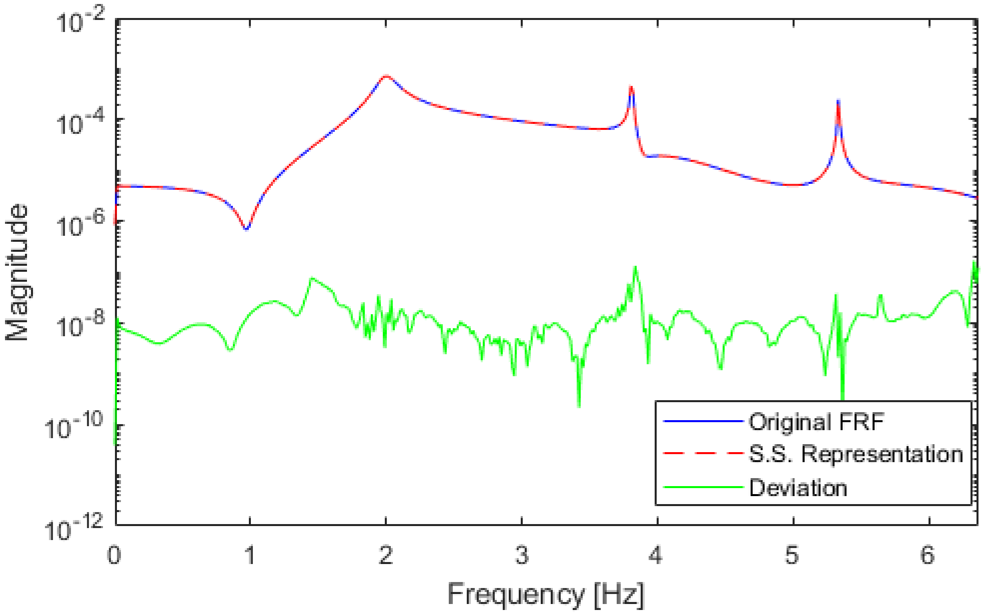

Figure 3.9: Fit of the state space representation of the pitch radiation coupling term compared to the FRF.

Here, the response does not align as well as in the previous two cases. However, the greatest amount of error at a given point in time is 3%. It is evident from the residuals in Figure 3.9 that the state space representation fits the data relatively well. The error likely comes from the increased dynamic complexity of this specific FRF. This kind of error is acceptable for FlOWCITSS, especially considering the increased computation time and burden of formal numerical convolution integration in a block diagram. The shape and magnitude of the time response is very similar, thus it should produce a similar response when used in the block diagram. Furthermore, the adequacy of the state space realization will be further tested in Chapter 4, when the model as a whole is validated against experimental results.

Similarly to the radiation coupling term, FlOWCITSS represents the radiation impedance term, $Z_{j,j'}$, as

$$Z_{j,j'} = R_{j,j'} + i\omega[a_{j,j'} - a_{j,j'}(\infty)], \tag{3.8}$$

where $R_{j,j'}$ is the radiation damping and $a_{j,j'}$ is the added mass coefficient [32]. FlOWCITSS uses this form to input the radiation impedance term into vecfit3 to evaluate the state space realization.

FlOWCITSS finds the state space realizations of all FRFs by using vecfit3. The block diagram that uses these state space representations is explained in the following section.

### 3.3.3 Block Diagram Formulation

With the outputs from WAMIT processed into FRFs and state space representations, one can now solve the mathematical model described in Chapter 2. Due to the complexity and the components involved in the mathematical model, FlOWCITTS uses a block diagram to facilitate finding a numerical solution. The mathematical model and a bond graph that Kurniawan used in his simulations of floating OWCs informed the basic structure of the block diagram, shown in Figure 3.10 [23]. The volume flow, body force, mooring forces, and turbine flow equations are separate subsystems that interact with each other. The nature of these coupled equations lends itself well to block diagrams, since they systematically iterate through time and some systems, like the mooring model, can iterate to find an appropriate value within a time step.

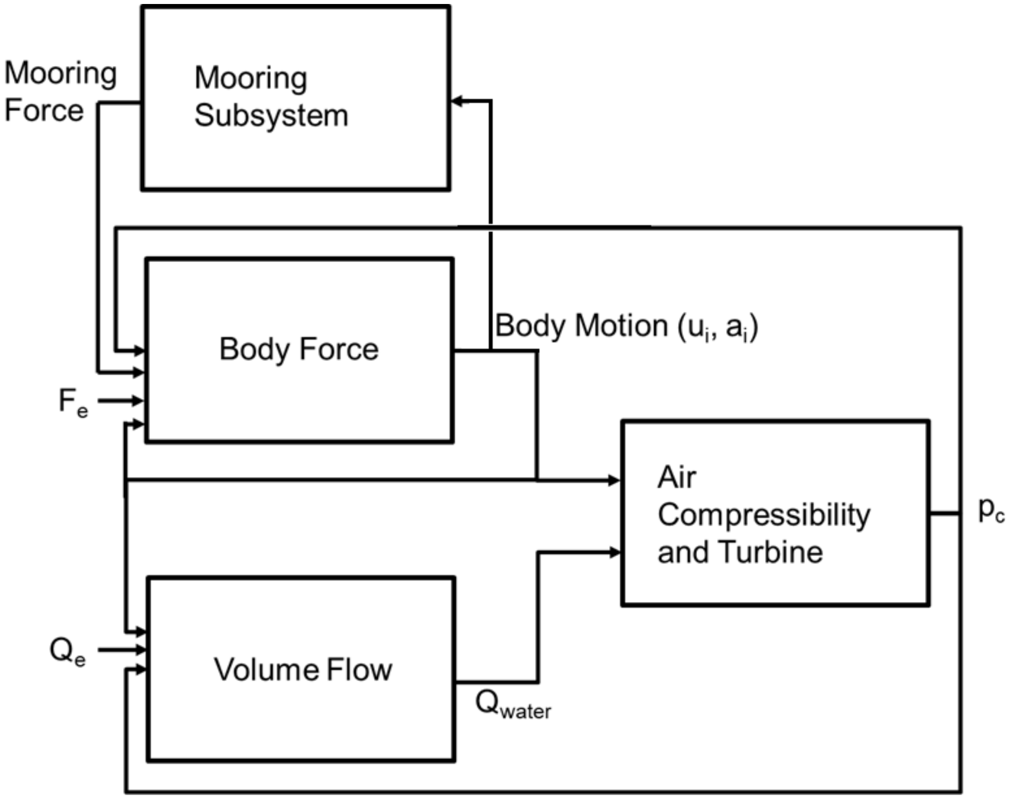

Figure 3.10: A diagram that displays the flow of data between the different subsystems of the block diagram. $F_e$ and $Q_e$ are the excitation inputs for force and volume flow. The unknowns calculated in the system are the body motion variables [velocity ($u_i$) and acceleration ($a_i$)] in the $i$ body motion direction and the chamber pressure ($p_c$). The volume flow across the internal free water surface is represented by $Q_{water}$.

Each block in Figure 3.10 is detailed and explained below, starting with the volume flow block in Figure 3.11. This subsystem uses the body velocity in all degrees of freedom, the chamber pressure, and the excitation volume flow to determine the volume flow across the internal free surface. A separate radiation coupling term and $C(\infty)$ term exists for each body motion direction considered. The state space representation of the radiation coupling term used here is the same representation used in the body force block.

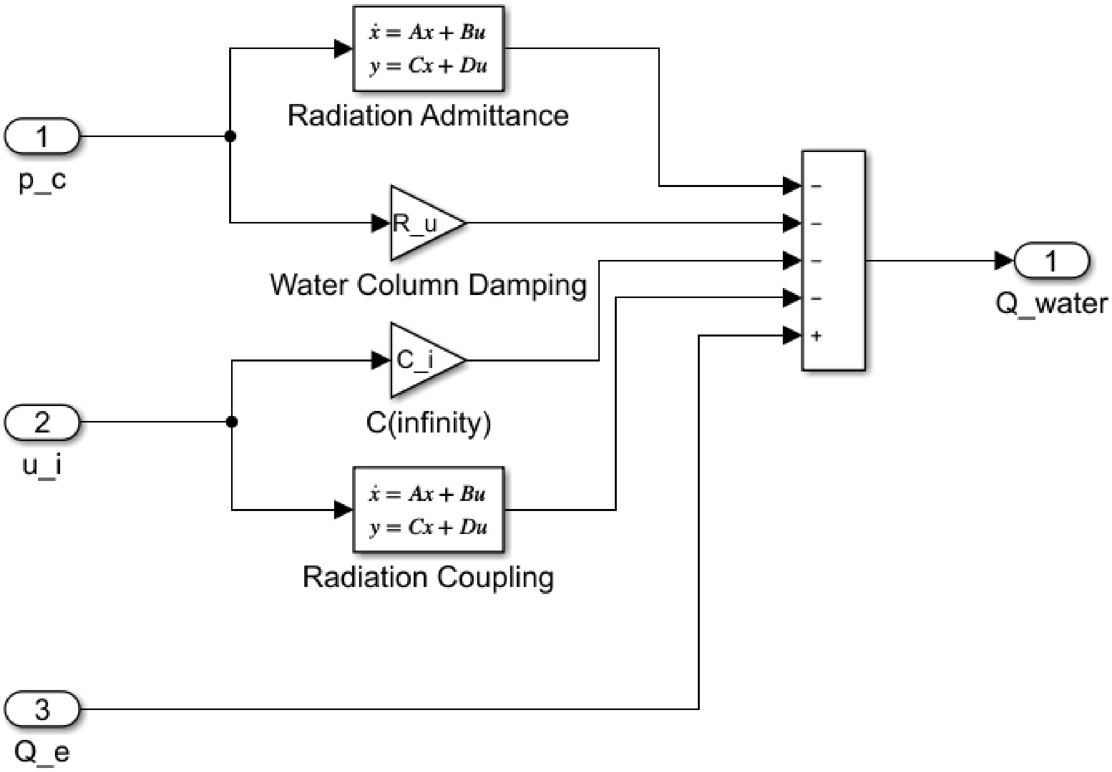

Figure 3.11: This diagram represents the volume flow block from Figure 3.10.

The body force block in Figure 3.10 is detailed in Figure 3.12. One of these blocks exists for every body motion direction considered. The primary inputs to the subsystem are the chamber pressure, and the body velocity and acceleration for all directions of motion. $u_i$ and $a_i$ indicate the body velocity and acceleration associated with the direction of force currently being calculated. $u_j$ and $a_j$ indicate the body velocity and acceleration associated with all body motion directions in the system, including the one currently being evaluated. The system outputs the body velocity and the body acceleration in one direction.

Before the addition junction in Figure 3.12, the integration block uses the trapezoidal method to find the body displacement [40]. After the addition junction, FlOWCITSS finds body acceleration by dividing by the body's mass or moment of inertia, depending on the degree of freedom. Then, FlOWCITSS finds the body velocity by integrating using the same trapezoidal integration block that was previously used to find body displacement.

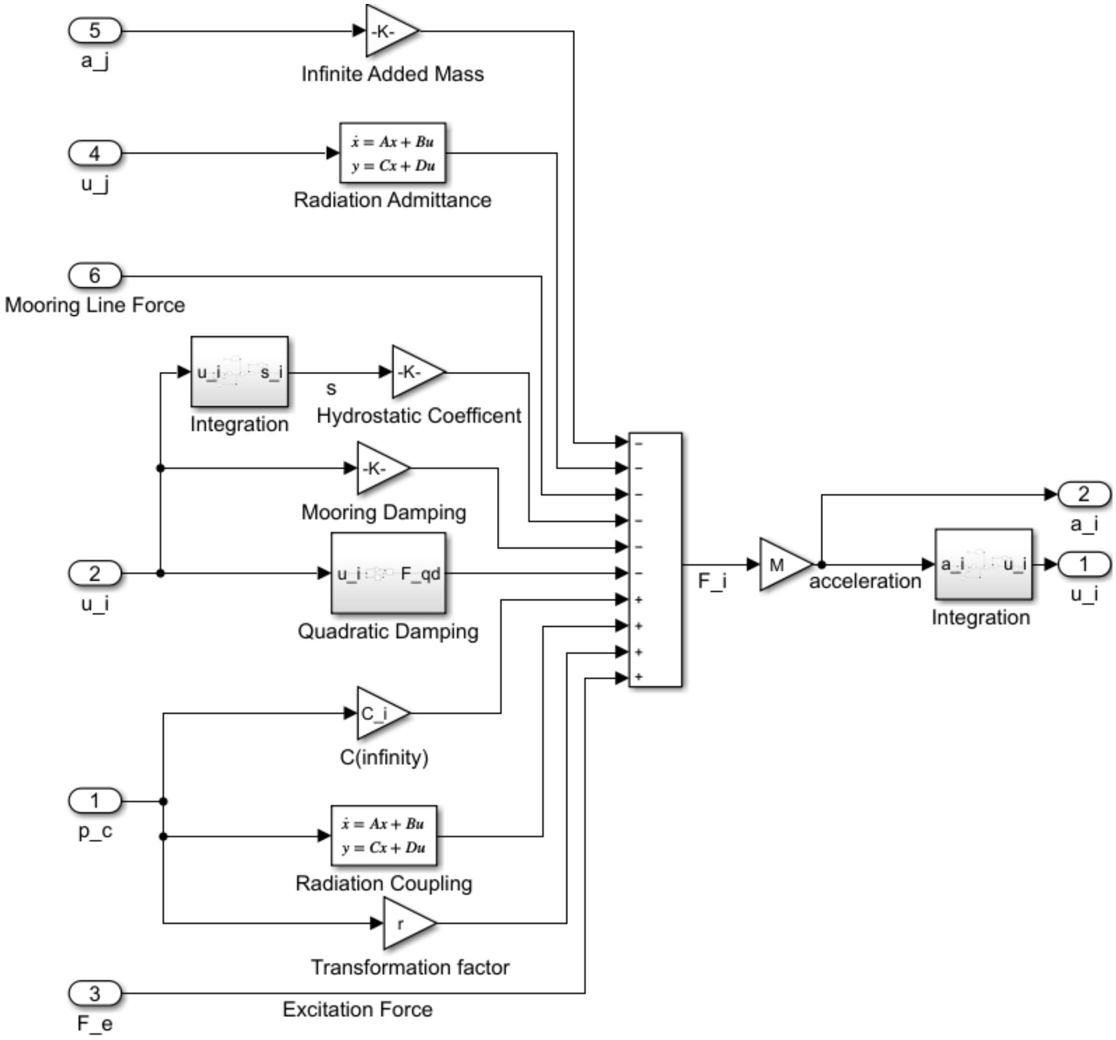

Figure 3.12: This diagram represents the body force block from Figure 3.10.

The mooring line force in Figure 3.12 comes from the mooring subsystem block in Figure 3.10. This mooring line subsystem is shown in Figure 3.13. Here, FlOWCITSS inputs all of the user defined mooring parameters into the block. The line length is the total length of the mooring line, moorDepth is the initial vertical distance between the bottom of the ocean and the location where the mooring line attaches to the body, x0 is horizontal distance between the location where the line attaches to the body and the mooring anchor on the bottom of the sea floor, and alphain is the initial guess for $\alpha$ in Equation 2.14, which is based on the $\alpha$ value from the previous time step. The main function block that all of the inputs go into is a MatLab script that conducts a Newton-Raphson iteration to find the horizontal mooring tension at the body's new position. The iterative process consists of finding $\alpha$ by

$$\alpha_{j+1} = \alpha_j - \frac{f\left(\alpha_j\right)}{f'\left(\alpha_j\right)} \tag{3.9}$$

$$f\left(\alpha_j\right) = \sinh\left(\alpha_j\left(\sqrt{h\left(h+\frac{2}{\alpha_j}\right)}+\ell'-\ell_T\right)\right) - \alpha_j\sqrt{h\left(h+\frac{2}{\alpha_j}\right)} \tag{3.10}$$

$$\begin{aligned} f'\left(\alpha_j\right) = & \frac{\left[h\left(\alpha_j+1\right)+\alpha_j\left(\ell'-\ell_T\right)\sqrt{h\left(h+\frac{2}{\alpha_j}\right)}\right]\cosh\left(\alpha_j\left(\sqrt{h\left(h+\frac{2}{\alpha_j}\right)}+\ell'-\ell_T\right)\right)}{\alpha_j\sqrt{h\left(h+\frac{2}{\alpha_j}\right)}}, \\ & -\frac{h\left(\alpha_j h+1\right)}{\alpha_j\sqrt{h\left(h+\frac{2}{\alpha_j}\right)}} \end{aligned} \tag{3.11}$$

where all of the variables are consistent with those defined in the Mooring section in Chapter 2 [14]. Within a single time step, this function block calculates $\alpha_{j+1}$ using the $\alpha_j$ from the previous iteration step and the values from Equations 3.10 and 3.11. Then, this function block compares the difference between $\alpha_{j+1}$ and $\alpha_j$. When this difference is below a user specified threshold, which in this body of work is 0.00025, the iterative process completes and the function block outputs the final $\alpha$ value, which is then used to calculate the horizontal and vertical tension of the mooring line using Equations 2.15 and 2.16. When one has multiple mooring lines, one can implement multiple versions of these blocks in the diagram.

Then, the resulting tensions are summed together to determine the total force being applied in each body direction.

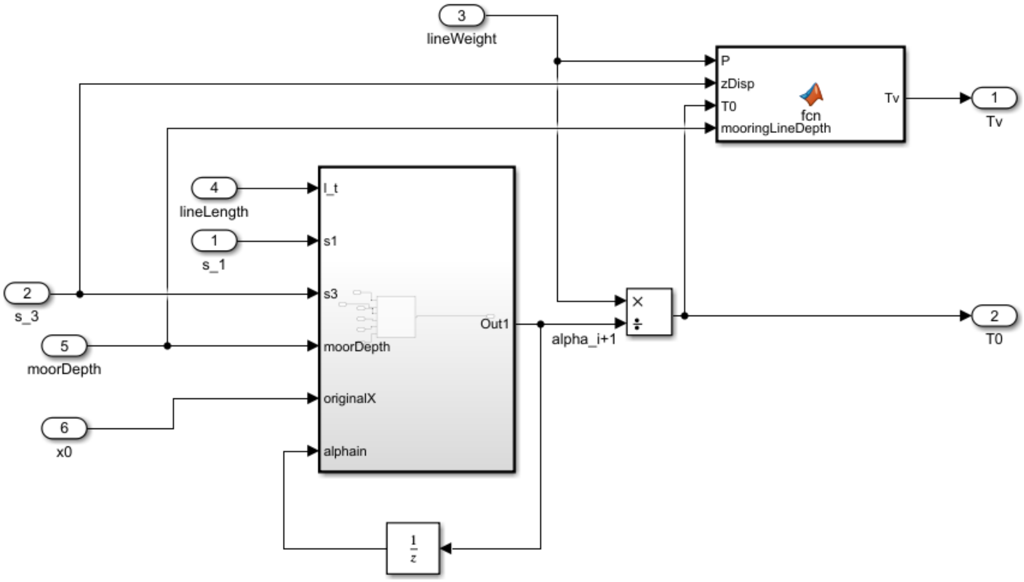

Figure 3.13: This diagram represents the body mooring subsystem block from Figure 3.10. $s_3$ represents the body displacement in the heave direction and $s_1$ represents the body displacement in the surge direction.

The last block in Figure 3.10 is the block that takes into account air compressibility and turbine dynamics. This block is shown in detail in Figure 3.14. Before FlOWCITSS can determine the chamber pressure, this subsystem must first find the current volume in the air chamber and the change in volume over time at the current time step. This happens by simultaneously considering the body velocity and the water column volume flow. FlOWCITSS then uses the volume and the change in volume over time as inputs for the air compressibility block, which uses Equations 2.19 and 2.20 to determine the chamber pressure and the volume flow across the turbine.

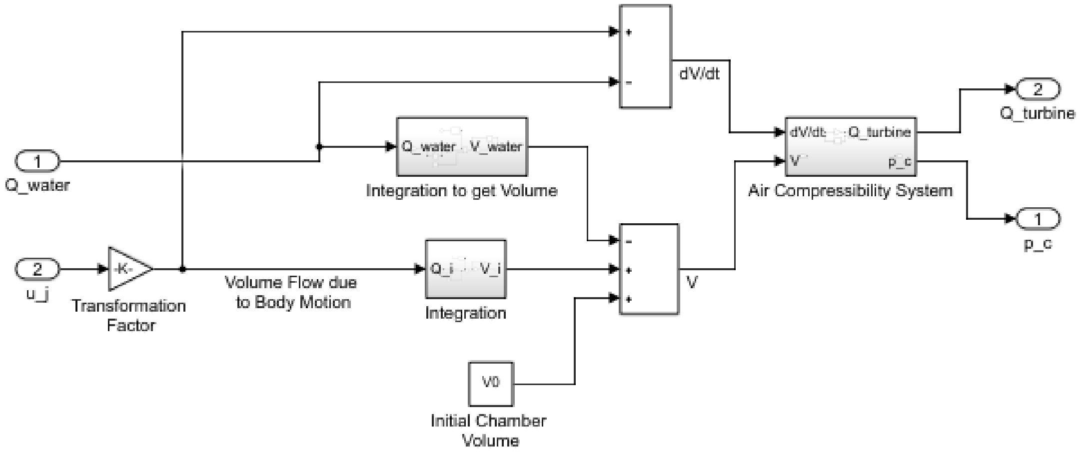

Figure 3.14: A diagram explaining how the air compressibility and turbine block from Figure 3.10 operates.

All of these blocks and subsystems combine to simulate device dynamics holistically and consider the complexly coupled dynamics of a floating OWC. In order to prove the accuracy of this model and the applied techniques, the next chapter validates the model against experimental results.

# Chapter 4

# Simulation Validation Against Published Experiments

## 4.1 Description of Experiment

The experimental results used in this body of work were collected by Minghao Wu from the University of Ghent and published in the open-access journal, Energies [46]. He conducted the experiments in a shallow wave flume using two different geometries, shown in Figure 4.1. Wu secured each geometry to the bottom of the tank using a multi-catenary mooring system. Figure 4.2 shows the testing and instrumentation set up.

Due to the geometry and the mooring system evaluated in this experiment, these experimental results are ideal to compare to results simulated in FlOWCITSS. Additionally, Minghao Wu shared his data files for two different incidents waves per geometry, which allows for a better comparison between simulated and experimental results.

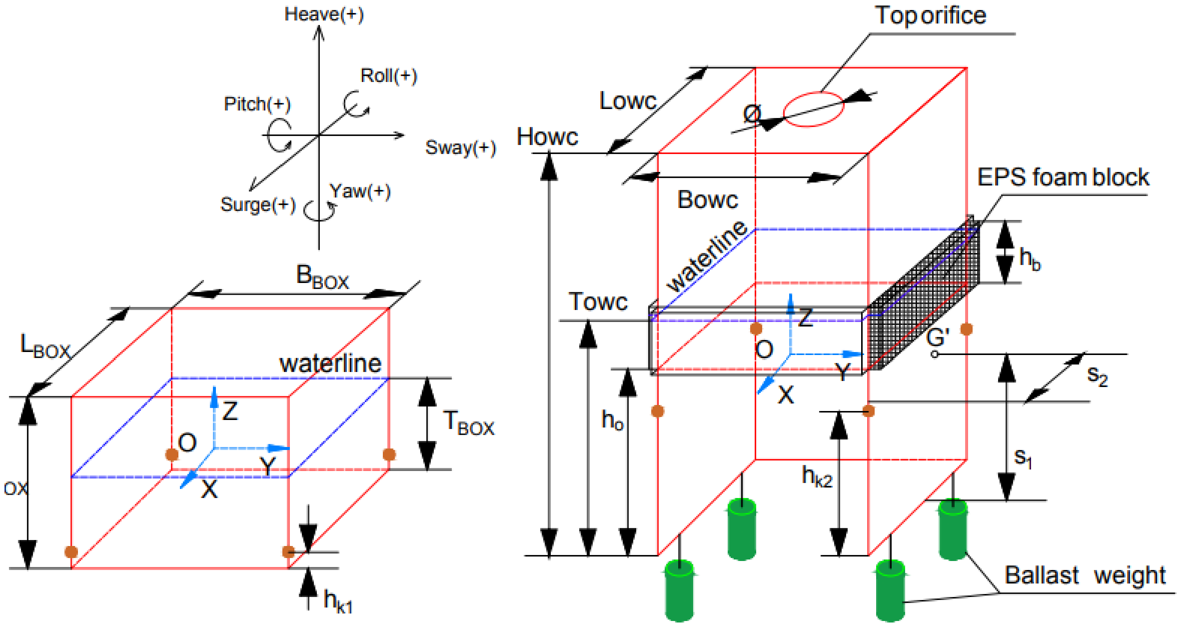

(a) (b)

Figure 4.1: Diagrams of experimental floating geometries, where geometry a is a box and geometry b is a floating OWC [46].

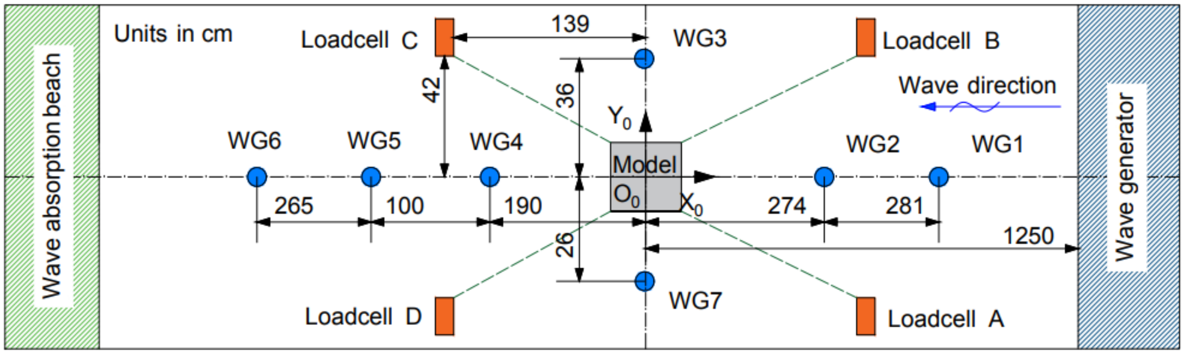

Figure 4.2: Diagrams of experimental set up in the shallow wave channel, including locations for load cells to monitor the mooring lines and the instrumentation for monitoring water elevation [46].

## 4.2 Methodology for Simulating Experimental Tests

For each geometry in Figure 4.1, FlOWCITSS will simulate 2 test cases, each using the same chain mooring configuration and water depth, but with a different incident wave. The floating moored box will help validate the adequacy of the body forcing components in the model while the floating OWC will help validate the coupled dynamics between the internal water column volume flow, chamber pressure, and the body's motion.

The first test case of each geometry is used to tune parameters that are not provided experimentally, such as mooring damping coefficients and the resistance across the air chamber orifice. The tuning process involves estimating the values for each parameter based on literature and theory, running the simulation, observing the dynamic response, and then updating the parameters until the simulated response matches the experimental response. Then, FlOWCITSS evaluates the second test case with the tuned parameters from the first test case. The purpose of doing this is to try to account for uncertainties in the simulation and the experimental setup.

Each geometry is modelled using Multisurf. Then, WAMIT uses the higher order panel method, irregular frequency removal, and logarithmic singularity removal options to evaluate the hydrodynamic and hydrostatic coefficents. WAMIT evaluates each geometry for frequencies ranging from 0-30 rad/s, with a step size of 0.1 rad/s. WAMIT evaluates the floating OWC for wave headings ranging from 0-180 degrees, with a step size of 5 degrees. The frequency range was determined based on how quickly the excitation force FRFs decayed to zero. The floating box is only evaluated for the 0 degree wave heading, since there is no internal water surface that would require a larger wave heading range.

For both cases, the incidental wave data from the experiment is evaluated in order to determine the period and height of the incident wave. This period and wave height are then used to model a theoretical linear wave of the form $\eta = A\cos\omega t$, where $\eta$ is the wave elevation, $A$ is the wave amplitude and $\omega$ is the frequency. The excitation inputs to the model are generated from this theoretical wave. The validation process uses a theoretically modelled incident wave since the fluid velocity can more easily and accurately be determined using wave theory. Fluid velocity significantly impacts drag forces, which can have a large effect on the body's motion. Since fluid velocity changes depending on the location in the fluid and vary with time, and since fluid velocity is generally larger than the body velocity, it is important to ensure that the phase and magnitude of the fluid velocity aligns appropriately with the incident wave.

## 4.3 Methodology of Error Evaluation

To determine how accurately FlOWCITSS predicts the motion of the body and the internal water column, one must compare simulation results to experimental results. Since the ultimate goal of the modeling tool is to predict pneumatic power performance, the most important responses are the volumetric flow across the internal free surface and the heave motion of the body. These two responses are the most important because they are the dominating inputs when it comes to volumetric flow across the turbine, which directly relates to pneumatic performance. Body motion in other directions, like surge and pitch, do contribute to power generation, but do not provide as significant of a contribution. These directions are also important to model because of how these degrees of freedom relate to heave motion and volumetric flow.

A relative error norm can be calculated by

$$\text{Error} = |\frac{y - \hat{y}}{y}|, \tag{4.1}$$

where $y$ is the averaged experimental metric and $\hat{y}$ is the averaged simulated metric. This error evaluation can be applied to the device response in multiple degrees of freedom and for different metrics. Several metrics of interest are the steady state period and height of the response for body displacement in each direction and the internal water surface elevation. Only the steady state period and height are evaluated, since the steady state response of a WEC is what is most salient to power generation.

To determine the steady state height and period of the response, these metrics are averaged across several response cycles. The period is calculated by measuring the time between response peaks, and the height is calculated by measuring the distance between the peak and the trough of the response. The rigor of these error evaluations reflects the fidelity of the model and the goals of the evaluation: to easily get a sense of what the pneumatic power performance of different floating OWCs may be.

## 4.4 Floating Moored Box

This section will review the results from the moored floating box simulation and compare them to the experimental results. The first test case analyzed is for a wave period of 1.6 s and a wave height of 0.11 m, shown in Figure 4.3. This test case is the tuning test case. The tuned parameters are the damping coefficients from the mooring model, whose final values are represented in Table 4.1.

Table 4.1: Tuned Metrics for the Floating Box

| Parameters | Values |
|---|---|
| Heave mooring Damping | 0.001 $\frac{Ns}{m}$ |
| Surge mooring Damping | 0.001 $\frac{Ns}{m}$ |
| Pitch mooring Damping | 0.5 $\frac{Ns}{\text{deg}}$ |

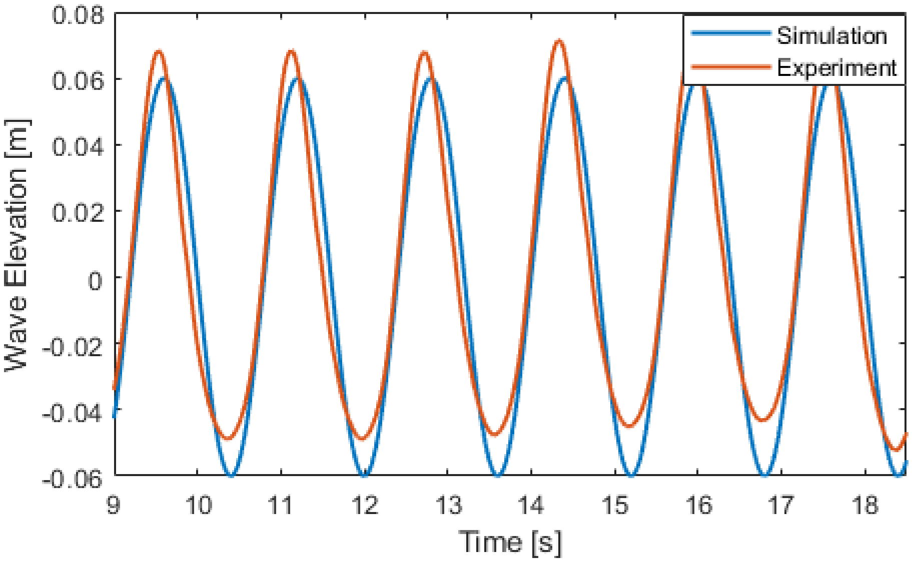

Figure 4.3: The theoretically modeled incident wave compared to the wave elevation from the experimental results for the floating box tuning case.

Although the steady state wave height and period are the same for the theoretically modeled wave and the wave elevation data, the input incident waves are not identical. The experimental wave data is centered on some positive value above zero, while the theoretically modelled wave is centered on zero. These differences could impact the accuracy of the solution, especially considering hydrostatic forces and mooring, both of which are dependent on the displacement in heave to determine restoring forces.

Figures 4.4 - 4.6 show the difference between the experimental results and the simulated results in heave, surge, and pitch. Table 4.2 shows the error associated with the tuning case for the floating box model.

Across the board, the period of the simulated response matches pretty closely with the experimental results; the error does not exceed 1% in any direction for the response period. The general shape of the simulated surge and heave responses matches fairly well with the experimental results. They both have a consistent, single frequency, sinusoidal response. However, the height of these simulated responses do vary from the experimental results. The height of the surge response has an error of 13.17% while the height of the heave response has an error of 6.8%. These errors are not ideal, but FlOWCITSS still captures the general behavior of the device response in heave and surge. FlOWCITSS does not capture the pitch response quite as well, as seen in Figure 4.6. While FlOWCITSS captures the dominant frequency and oscillatory behavior, it does not have the same shape as the experimental response. The experimental data appears to have other frequencies in the response. There is the possibility that these other frequencies appear due to the data capture methods that the experiment used. Wu mentioned that the data collection system could introduce uncertainties and error into the simulation. The mooring restoring forces and damping could also contribute to the discrepancies in the pitch response.

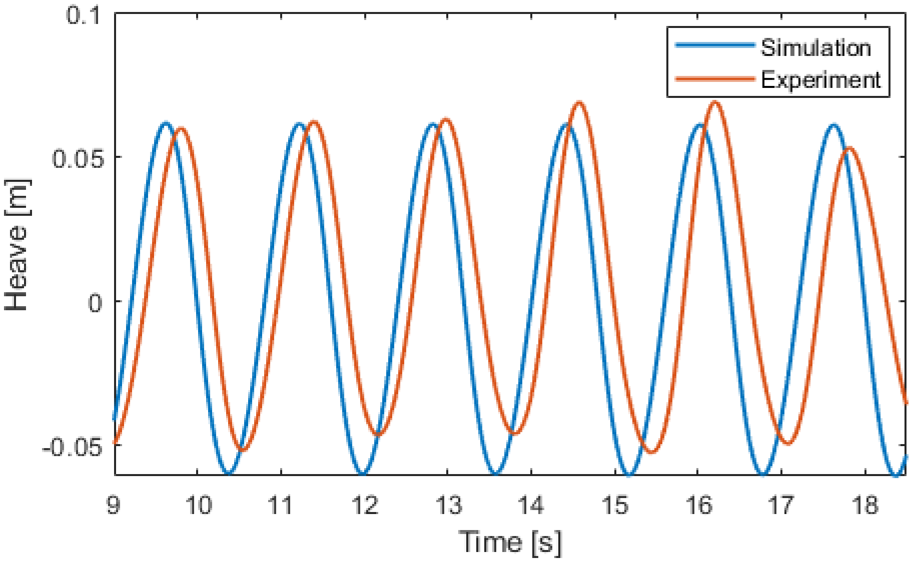

Figure 4.4: A comparison of the simulated heave response to the experimental heave response for the floating box tuning case.

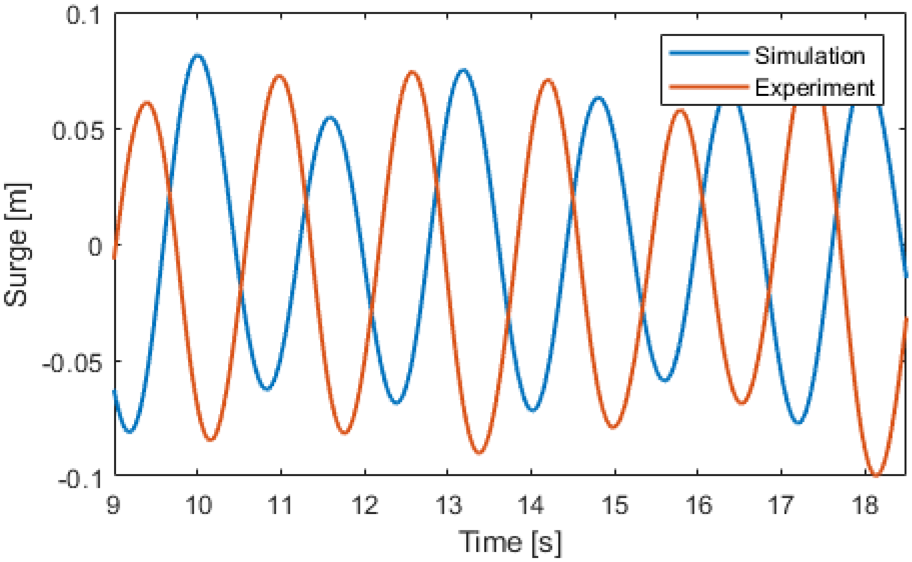

Figure 4.5: A comparison of the simulated surge response to the experimental surge response for the floating box tuning case.

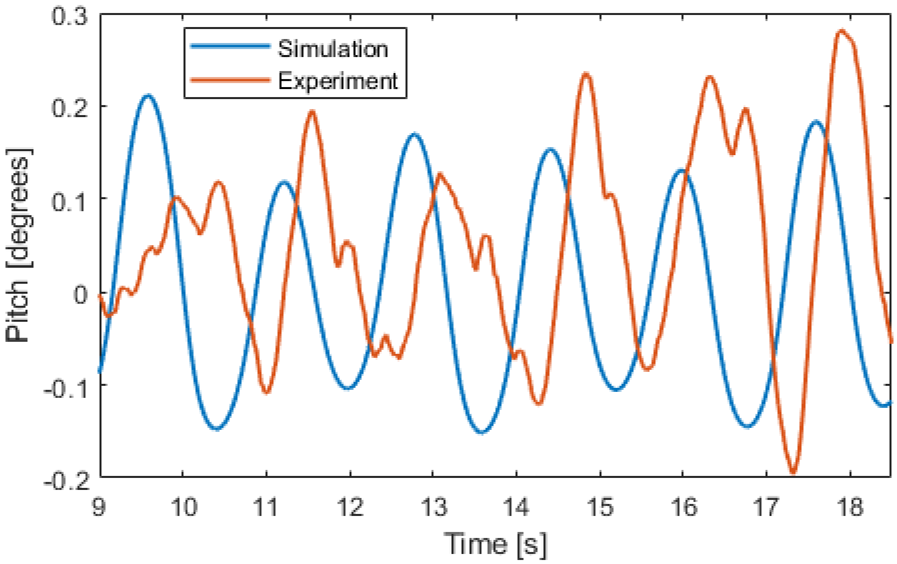

Figure 4.6: A comparison of the simulated pitch response to the experimental pitch response for the floating box tuning case.

Table 4.2: Error for Floating Box Model Tuning Case

| Response | Period Error | Height Error | Phase Shift |
|---|---|---|---|
| Surge | 0.102% | 13.17% | $0.75\pi$ rad |
| Heave | 0.279% | 6.8% | $0.19\pi$ rad |
| Pitch | 0.692% | 8.06% | $0.55\pi$ rad |

Using the tuned parameters from the first test case, FlOWCITSS simulates the effects from a different incident wave. This wave, shown in Figure 4.7, has a period of 1.8 seconds and a height of 15 cm. As with the previous test case, the period and wave height are the same, although the incident waves are not identical. Due to the nature of the wave channel Wu used to test, taller waves have a more irregular shape. In Figure 4.7, the experimentally modelled wave has a relatively sharp peak, a rounded trough, and a wave height that is centered above the average water line. All of these differences between the theoretically modeled wave and the experimental wave can impact the simulated device response.

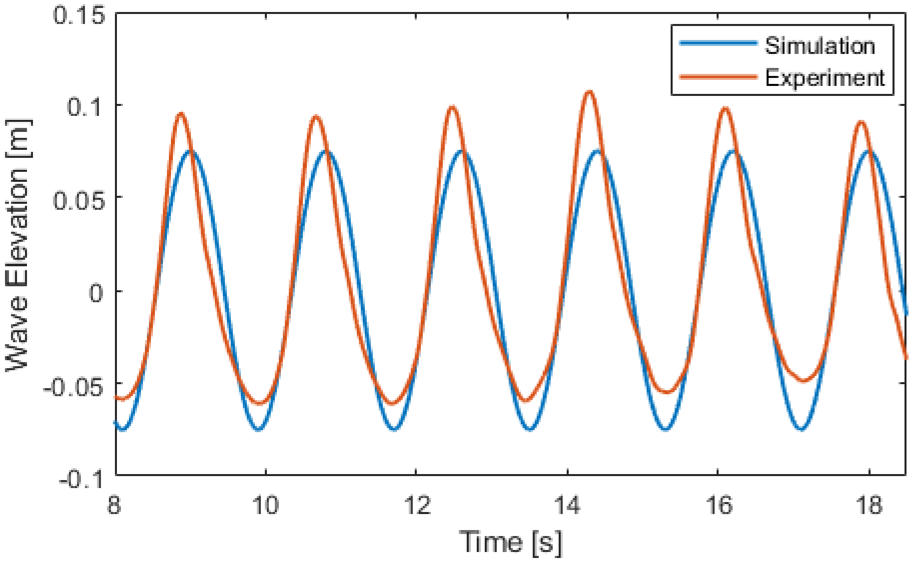

Figure 4.7: The theoretically modeled incident wave compared to the wave elevation from the experimental results for the floating box case using tuned parameters.

Figures 4.8 - 4.10 show the simulated response of the floating box using the tuned parameters compared to the experimental response. Table 4.3 shows the error of the simulated response when compared to the experimental response. In this case, FlOWCITSS appears to predict the heave response, shown in Figure 4.8, moderately well, with an error of less than 1% for the period and an error of 3.856% for the height. The shape here also appears to be relatively similar, as both the simulated and experimental results have relatively sharp peaks and troughs.

FlOWCITSS models pitch and surge with less accuracy in this case. The surge response's period error of 4.75% and height error of 18.41% is greater than the error in the tuning case. In Figure 4.5, the general shape of the simulated response is relatively similar to the experimental response, although the simulated response does have sharper peaks and troughs. The simulated pitch response is significantly different from the experimental results, with a large error in both the period and the height of the response. The shape of the experimental response is not consistent, thus determining what response is considered steady state was based on the time range from the heave and surge responses. These errors in pitch and surge could be due to how the mooring is modeled, due to viscous drag, or due to effects from device motion in other directions.

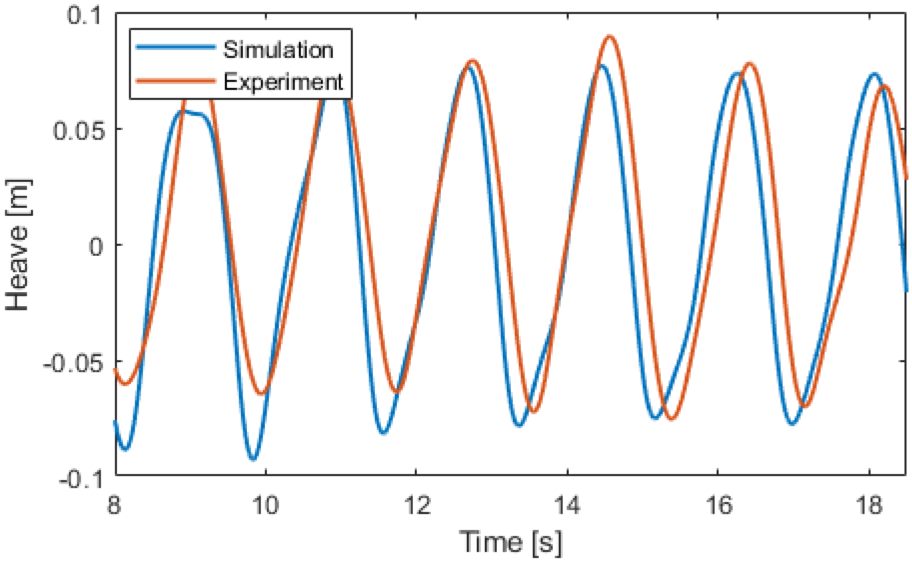

Figure 4.8: A comparison of the simulated heave response to the experimental heave response for the floating box case using tuned parameters.

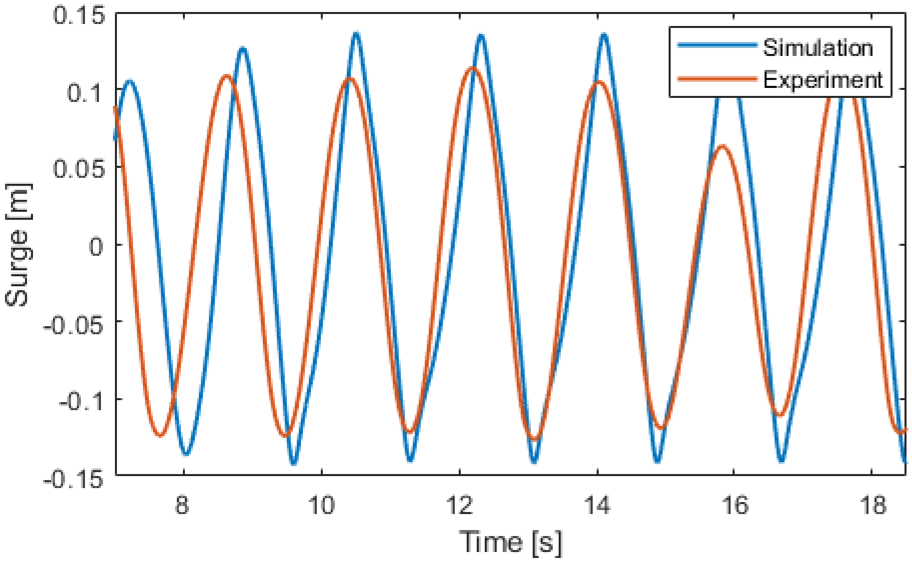

Figure 4.9: A comparison of the simulated surge response to the experimental surge response for the floating box case using tuned parameters.

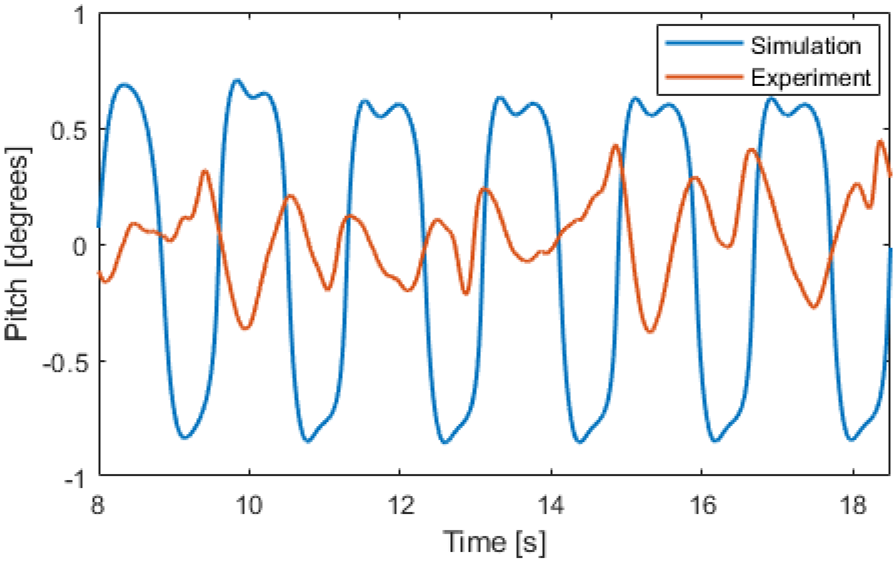

Figure 4.10: Comparison of simulated pitch response to experimental pitch response for the floating box case using tuned parameters.

Table 4.3: Error for Floating Box Model using Tuned Parameters

| Response | Period Error | Height Error | Phase Shift |
|---|---|---|---|
| Surge | 4.75% | 18.41% | $0.11\pi$ rad |
| Heave | 0.917% | 3.856% | $0.004\pi$ rad |
| Pitch | 51% | 165% | - |

The comparison between the simulated response and the experimental response for the floating box model indicates that the heave response, the most important motion when considering the power generation of floating OWCS, is able to be captured with some error in response magnitude. FlOWCITSS also appears to capture the general shape of the surge response with some errors in magnitude. The pitch response is the most inconsistently captured, given the differences in response shape, size, and period. These errors could be caused by the differences in the incident wave, the model used for the mooring lines, and the variation of fluid velocity across the surface of the box. For both cases, there was some phase shifting, particularly for the surge response. These phase shifts could be caused by the mooring model or by the viscous drag effects.

Observing how the simulated response of the floating box compares to the experimental results gives insight to the adequacy of the force equations and models when modeling a floating structure. In order to observe the coupled dynamics between the internal water surface and the body motion, the next section will compare the simulated response of the floating OWC to the experimental results.

## 4.5 Floating OWC Geometry

The moored floating OWC, geometry b in Figure 4.1, will help verify that the internal water column dynamics are adequately represented, and that the body motion and the chamber pressure are adequately coupled. These features directly contribute to power generation.

This device is first modeled in Multisurf utilizing symmetry along the y-z plane at $y = 0$. The modeled geometry, shown in Figure 4.11, is exported to WAMIT, where field points are distributed evenly across the internal free surface in a 10x10 grid. The outputs from WAMIT are then imported into FlOWCITSS.

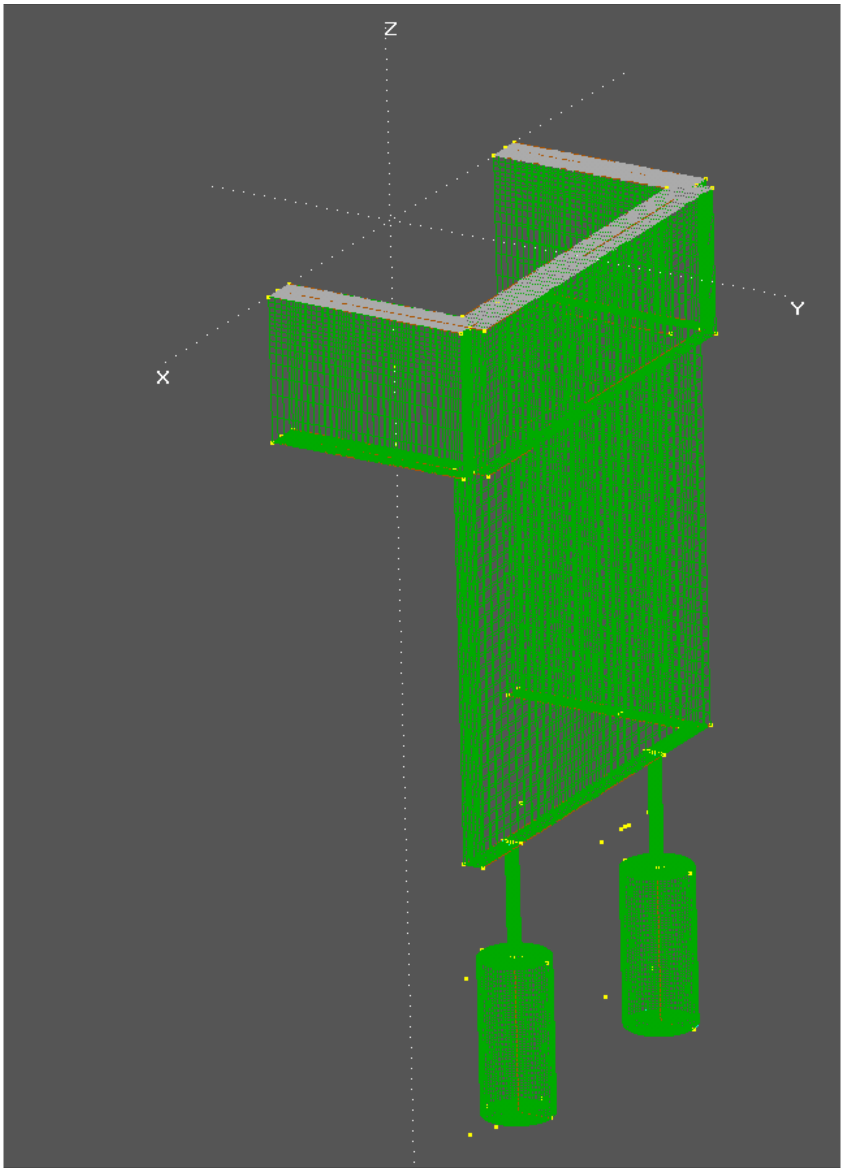

Figure 4.11: A model of the experimental floating OWC geometry created in Multisurf, utilizing symmetry along the y=0 plane.

Several sources of error and uncertainty in this process are: the effects that wave reflection from the channel walls have on the dynamic response of the body, drag coefficients of the body, mooring damping coefficients values, and the damping value of the internal water column. The experiment itself also introduces uncertainties such as: the moment of inertia of the body, errors in the motion tracking instrumentation, and the location and characteristics of the mooring line [46].

For this simulation, the mooring line damping, the drag coefficients, and the damping of the internal water column will be tuned based on the experimental result of one test case. The tuning process was very challenging due to the complex coupled nature of the system. Changing a parameter in one degree of freedom could affect the dynamic response in all degrees of freedom. The tuning test case consists of an incident wave with a period of 1.6 s and a wave height of 11 cm. The tuned parameters are shown in Table 4.4. The theoretically modelled wave is compared to the experimental wave data in Figure 4.12.

Table 4.4: Tuned Metrics for the Floating OWC

| Parameters | Values |
|---|---|
| Heave mooring Damping | $0.001\ \frac{Ns}{m}$ |
| Surge mooring Damping | $0.001\ \frac{Ns}{m}$ |
| Pitch mooring Damping | $4\ \frac{Ns}{\text{deg}}$ |
| Internal Water Column Damping | $1.5\frac{m^4s}{kg}$ |
| Turbine Loading Resistance | $4\frac{kg}{m^4s}$ |
| Heave Drag Coefficient | 1.3 |
| Surge Drag Coefficient | 2 |

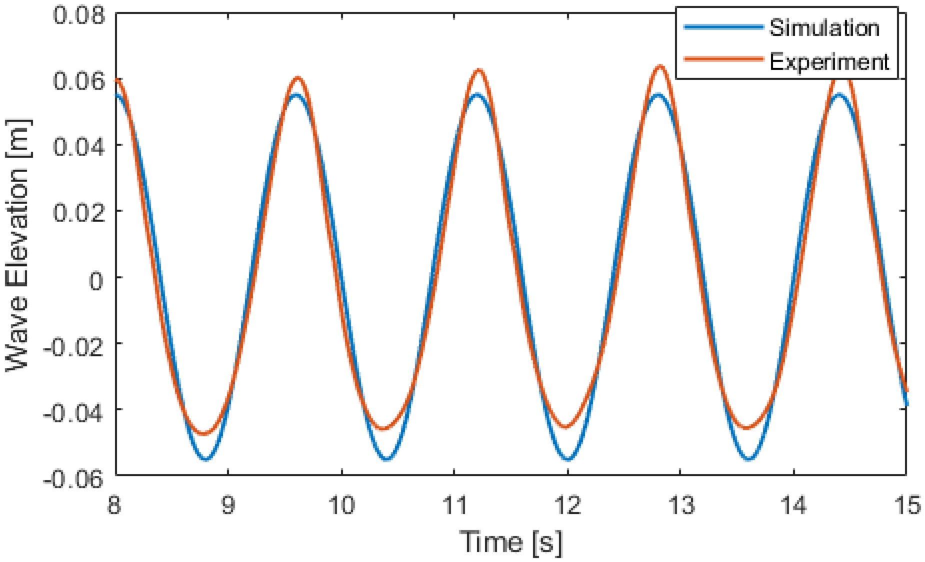

Figure 4.12: The theoretically modeled incident wave compared to the wave elevation from the experimental results for the floating OWC tuning case.

Figures 4.13 - 4.16 compare the simulated tuning case for the floating OWC with experimental results. Table 4.5 presents the errors associated with each response. The simulated heave and surge responses, shown in Figures 4.13 and 4.14, while having relatively low error for the period and similar shapes to the experimental response, have significant error in the height of the response, 33% and 25.6% respectively. The simulated pitch response, shown in Figure 4.15, is significantly different from the experimental results. There is a slight upward trend in the simulated pitch and it has a fairly consistent sinusoidal shape, while the experimental results are a bit irregular. The errors associated with this model could be caused by the uncertainties in device geometry and moment of inertia. Additionally, they could be caused by the variation in fluid velocity across the surface of the body, the mooring model, and the difference in incident wave inputs.

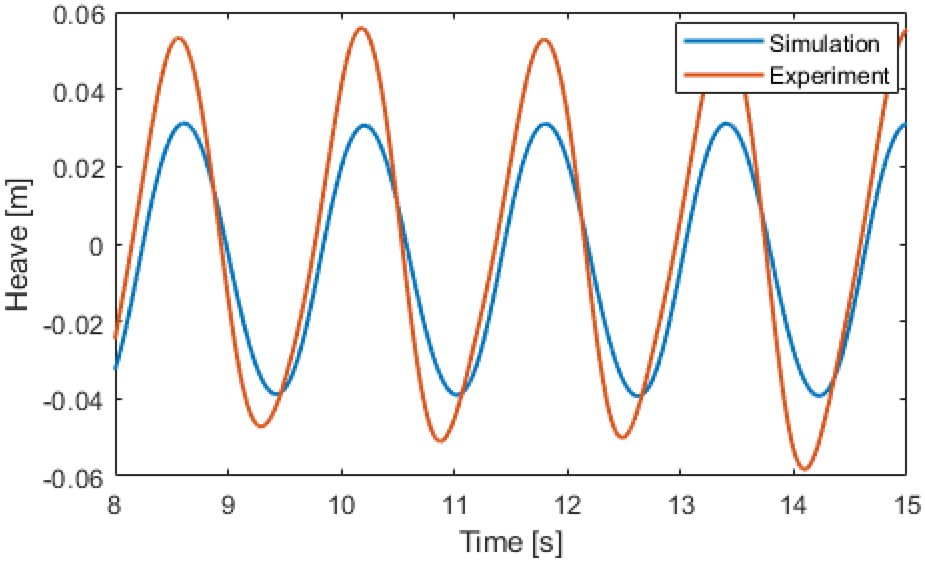

Figure 4.13: The simulated heave response compared to experimental results for the floating OWC tuning case.

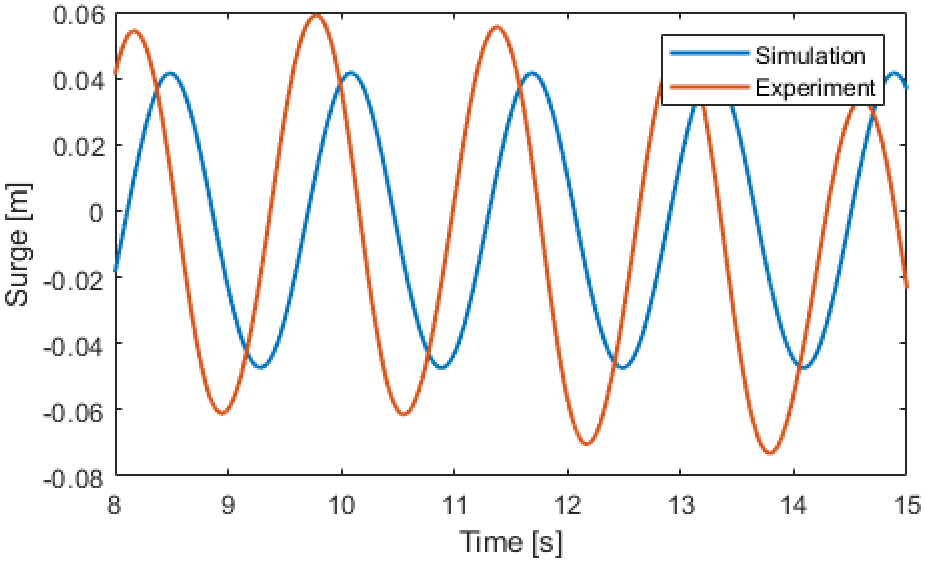

Figure 4.14: The simulated surge response compared to experimental results for the floating OWC tuning case.

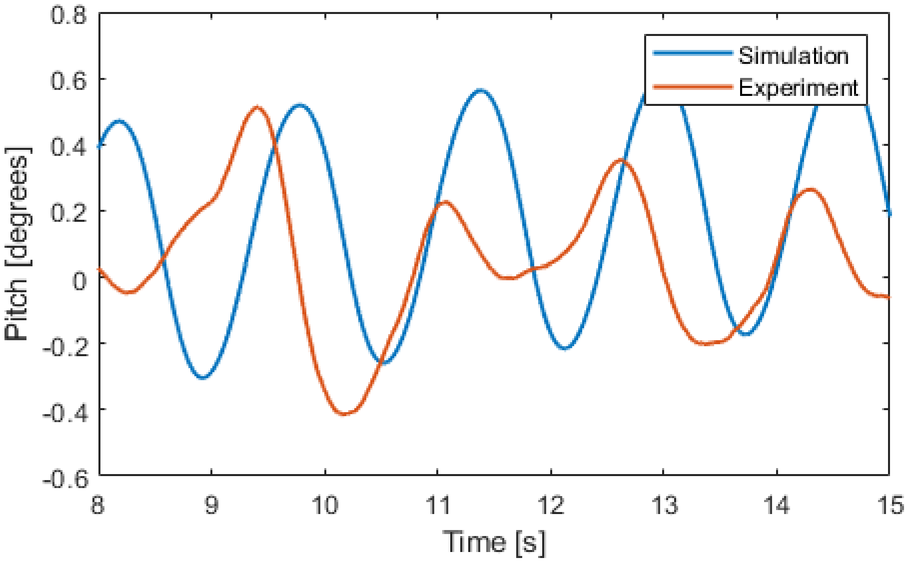

Figure 4.15: The simulated pitch response compared to experimental results for the floating OWC tuning case.

The experiment captures the internal water surface elevation relative to the heave motion of the body. Figure 4.16 shows the simulated internal surface elevation compared to the experimental results. The simulated response appears to capture the period and magnitude of the dominant frequency, given a period error of 0.44% and a height error of 1.56%. The internal water surface motion is a critical contributing factor in power generation of floating OWCs, so a lower degree of error here shows promise for FlOWCITSS's ability to predict some of the power generation capabilities of floating OWCs. However, the simulated response does not contain the second frequency that is evident in the experimental results. The reason why FlOWCITSS might be missing this secondary frequency could be because FlOWCITSS predicts the internal water surface elevation and the heave motion of the device as in phase with each other, when in reality, they might be slightly out of phase with each other. The reason for this phase issue could be because of how FlOWCITSS accounts for turbine dynamics. FlOWCITSS assumes a linear turbine at the air outlet, but the experiment does not have a turbine. The experiment accounts for some resistance by having a small hole at the top of the air chamber. The relationship between this resistance at the outlet, the volume flow across the outlet, and the chamber pressure is unknown, and could be the source of the phase issues seen here.

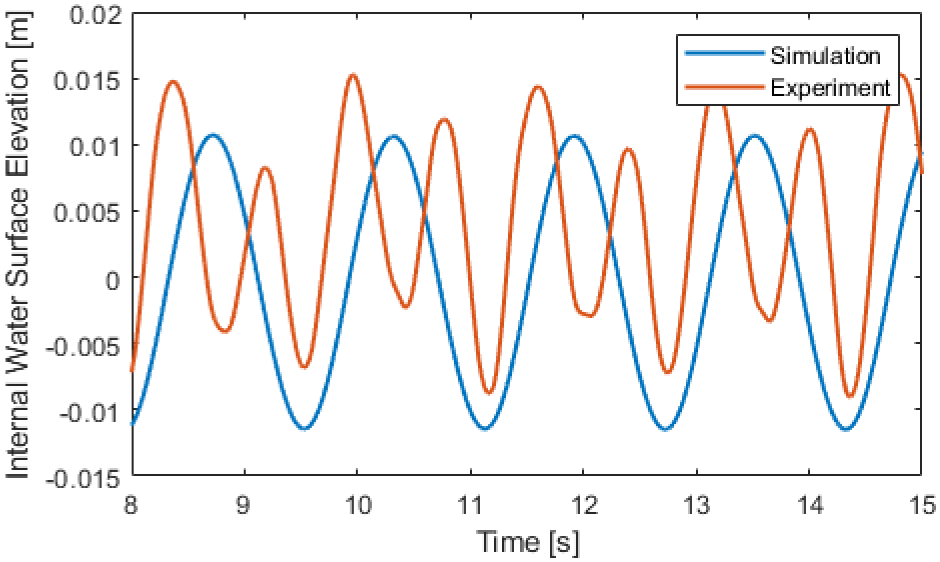

Figure 4.16: The simulated internal surface response compared to experimental results for the floating OWC tuning case.

Table 4.5: Error for Floating OWC Tuning Case

| Response | Period Error | Height Error | Phase Shift |
|---|---|---|---|
| Surge | 0.9207% | 25.6% | $0.4\pi$ rad |
| Heave | 0.251% | 33% | $0.03\pi$ rad |
| Pitch | 0.06% | 67% | $0.41\pi$ rad |
| Internal Water Surface | 0.444% | 1.56% | $0.44\pi$ rad |

Using the tuned parameters, FlOWCITSS will predict the response due to a different incident wave. This wave has a period of 1.9 s and a wave height of 14 cm, demonstrated in Figure

4.17. As with other cases, the experimental wave has sharper peaks and more rounded troughs than the theoretically modelled wave.

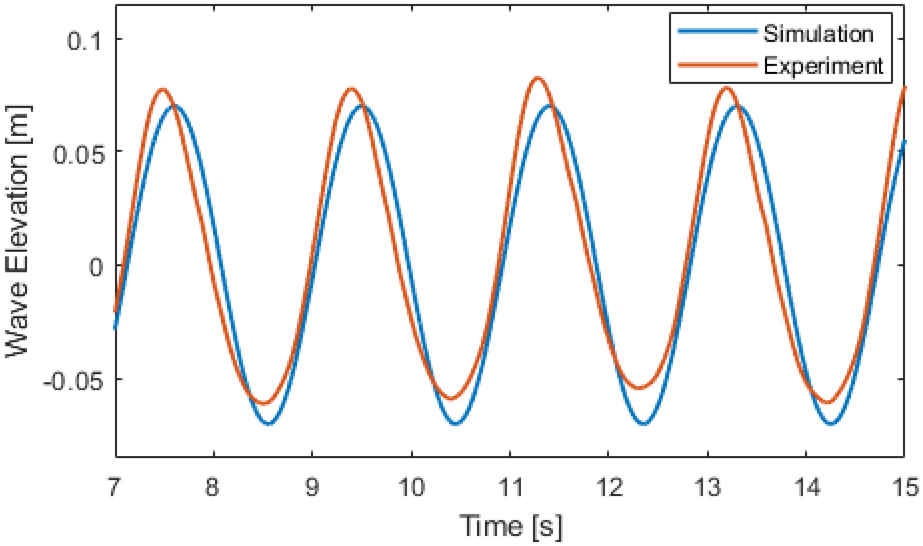

Figure 4.17: The theoretically modeled incident wave compared to the wave elevation from the experimental results for the second floating OWC case, using tuned parameters.

Figures 4.18 - 4.21 compare the simulated results to the experimental results, and Table 4.6 presents the errors associated with this case. The response height errors in this case are larger than the tuning case. For the simulated heave response, shown in Figure 4.18, the experimental response has an irregular shape compared to the simulated response. This is very likely caused by the difference in incident wave inputs. Additionally, there is a significant error of 37% in the the response height. The simulated surge response is similar to the experimental response, although it is slightly out of phase and has an error in height of 13.8%. The simulated pitch response, while matching relatively closely in period, has a significantly larger height and an a general upward trend.

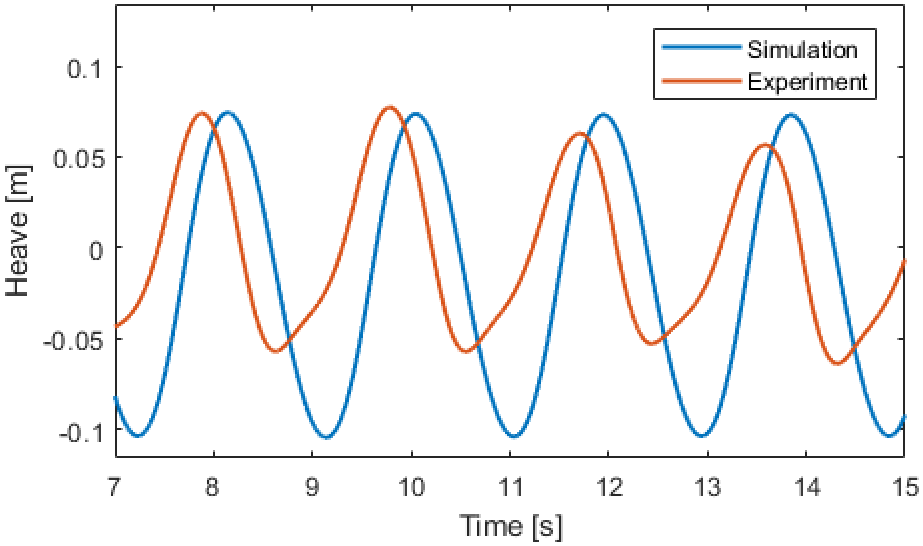

Figure 4.18: The simulated heave response compared to experimental results for the second floating OWC case.

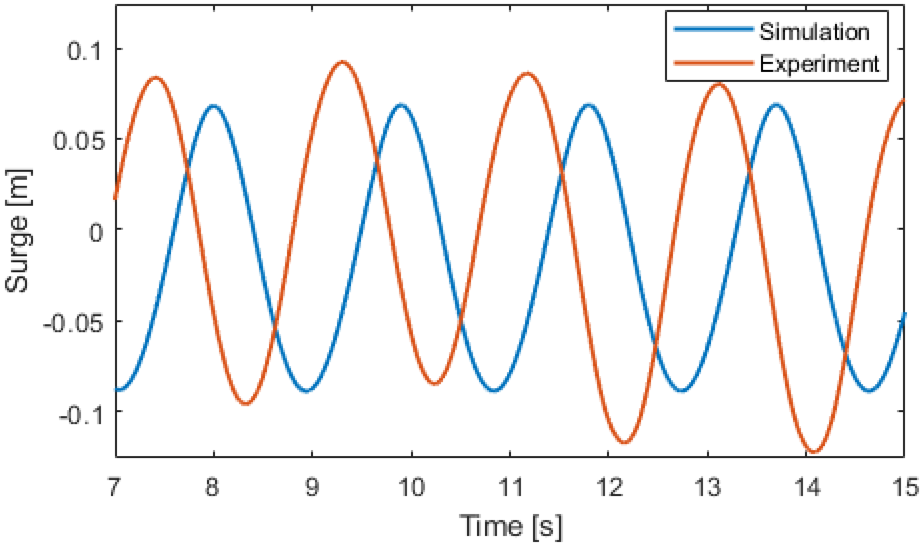

Figure 4.19: The simulated surge response compared to experimental results for the second floating OWC case.

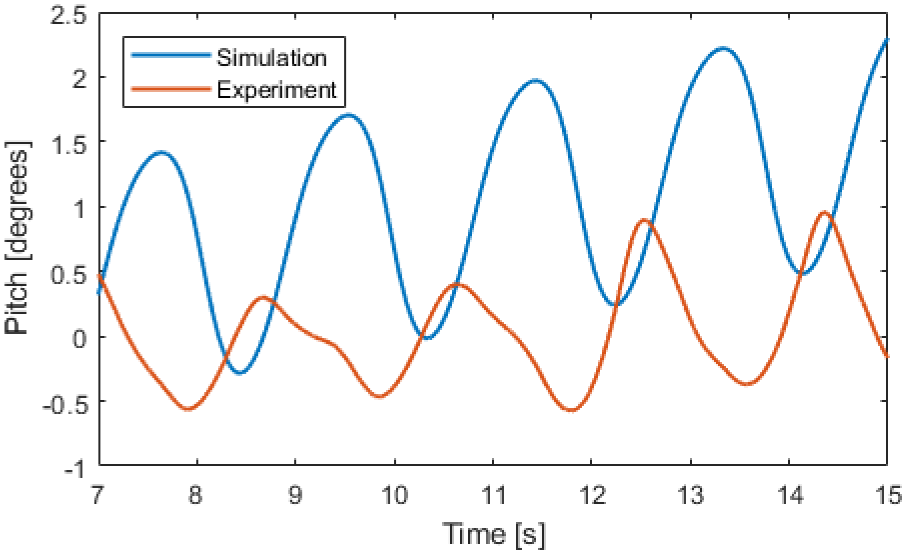

Figure 4.20: The simulated pitch response compared to experimental results for the second floating OWC case.

The simulated internal water surface elevation, shown in Figure 4.21, is distinctly different from the experimental results. As with the previous case, FlOWCITSS appears to only capture one frequency. However, the height of the response has an error of around 24%, which is significantly larger than the error of the previous case.

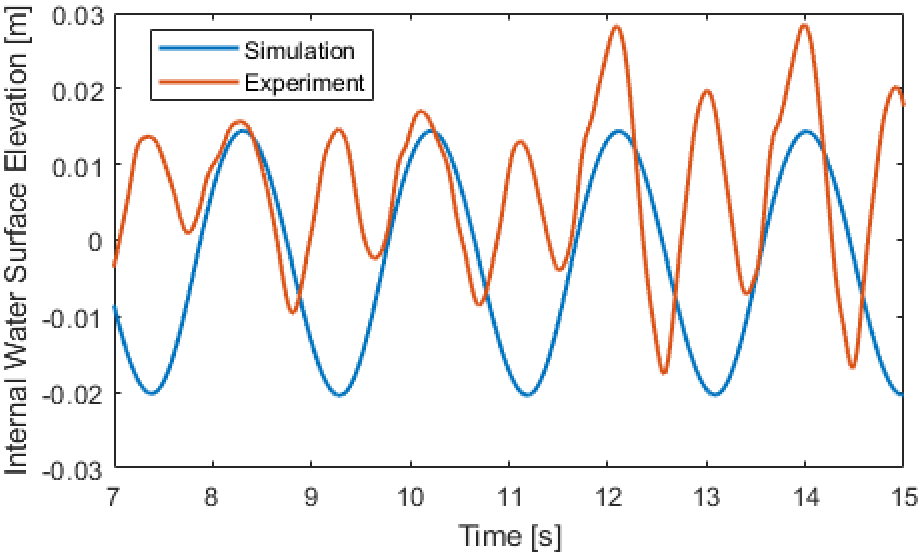

Figure 4.21: The simulated internal surface elevation compared to experimental results for the second floating OWC case.

Table 4.6: Error for Floating OWC using Tuned Parameters

| Response | Period Error | Height Error | Phase Shift |
|---|---|---|---|
| Surge | 0.1042% | 13.8% | $0.64\pi$ rad |
| Heave | 0.3979% | 37% | $0.25\pi$ rad |
| Pitch | 0.855% | 135% | $0.85\pi$ rad |
| Internal Water Surface | 0.7034% | 24.004% | $0.03\pi$ rad |

FlOWCITSS does not perfectly capture all device dynamics when simulating a floating OWC. However, it does capture some of the device dynamics, such as the oscillatory nature and period of the heave response, which is critical for estimating power generation. For both test cases, there was some phase shifting, particularly for the surge and pitch responses. These phase shifts could be caused by the mooring model or by the viscous drag effects and how the fluid velocity varies over the surface of the geometry.

The errors seen for the floating OWC geometry could be caused by the uncertainty in the experimental geometry and mass properties and the turbine modeling assumptions. In order to have a higher degree of certainty in the validation, a more well controlled experiment should be used as a point of comparison for FlOWCITSS.

These errors could also be caused by discrepancies in fluid velocity across the surface of the device, the mooring model, the estimated drag coefficients, the discrepancies between the experimental and the simulated incident wave, and the error introduced in using a state space realization in lieu of convolution integration.

## 4.6 Limitations of FlOWCITSS

The intended use of FlOWCITSS is for it to be an open access tool for the research community to use to explore different geometries, wave environments, turbine loads, and mooring configurations in order to determine which configurations are promising for a specific application. These promising configurations could then be analyzed using something with much higher fidelity, such as CFD analysis. While FlOWCITSS is a low fidelity tool, in the tool's initial conception, it does capture some aspects of device performance with varying degrees of error and with certain limitations.

One of the limitations is the ability for FlOWCITSS to consider only catenary mooring configurations. Additionally, FlOWCITSS does not appear to capture the pitch response of a device well, thus any WECs that rely heavily on pitch motion for power generation may not be well suited to this tool. FlOWCITSS currently considers only a linear turbine and uses a relatively simplistic air compressibility relationship. The drag model in the tool is also simplified, since it does not take into account a large degree of fluid velocity variation across the surface of the WEC geometry. With large devices, these fluid velocity discrepancies could contribute to more significant error than with smaller scale devices.

Additionally, FlOWCITSS, when analyzing these cases, used a fixed step size solver with a step size ranging from 0.0004 seconds to 0.00001 seconds. When the step size is larger, the results did not converge in Simulink. Using a step size this small did cause the simulation to take several hours to complete 15-19 seconds of simulated time using a personal computer. In future iterations of the tool, increasing the robustness or efficiency of the tool would be beneficial.

In order to demonstrate the use of this tool, the next section will present simulated results of several different BBDB geometries experiencing the same mooring configuration and wave environment.

# Chapter 5

# Demonstration of FlOWCITSS

To demonstrate the usefulness of FlOWCITSS, several floating OWC geometries will be simulated for the same wave conditions, turbine loading, and mooring configuration in order to see how different geometries affect performance. In this chapter, RM6 from Sandia National Laboratories is used as a base model for BBDB geometries. Then, by changing several different characteristics of RM6, variants of the BBDB emerge.

## 5.1 Geometries and Simulation Conditions

The wetted profile of RM6, shown in Figure 5.1, has several characteristics that, when changed, could impact power generation. Some of these characteristics include the shape of the stern, the angle of the water column opening, and the angle of the water column. Figure 5.2 shows the first variant, with a different stern geometry. Figure 5.3 shows the second variant, which has a different angle for the water column opening. Finally, Figure 5.4 shows the third variant, where the OWC varies in width and has an angle greater than 90 degrees to the air chamber. Given how device motion is complexly coupled in different degrees of freedom, and how WEC design prioritizes and encourages large responses, testing out different geometry configurations can improve the understanding of floating OWC power performance.

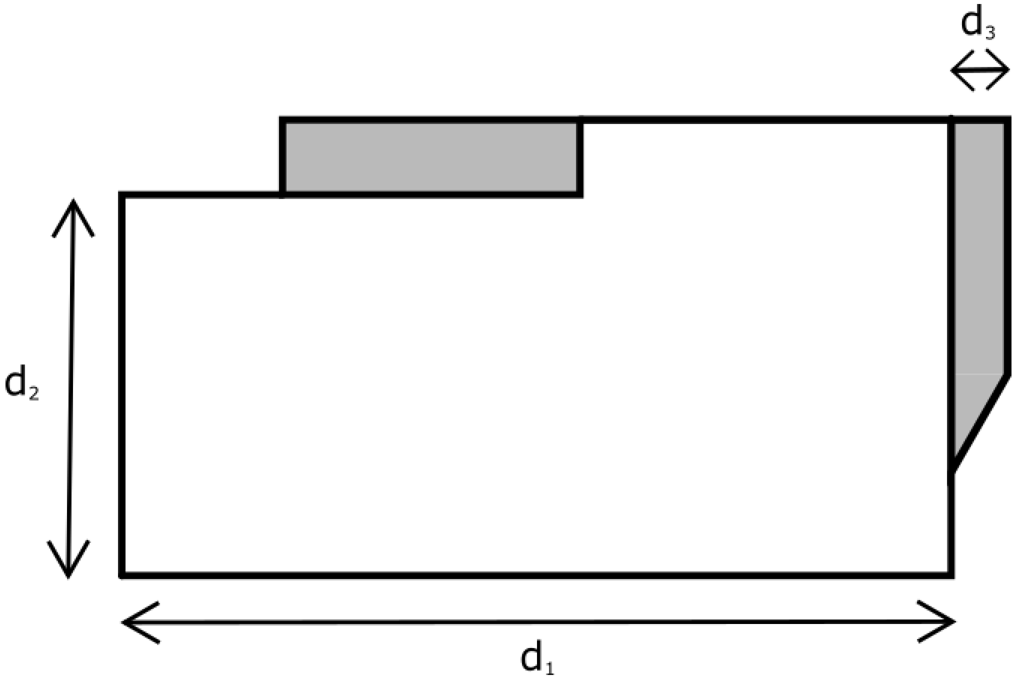

Figure 5.1: Wetted surface of RM6. $d_1 = 35m$, $d_2 = 17.5m$, and $d_3 = 2.7m$

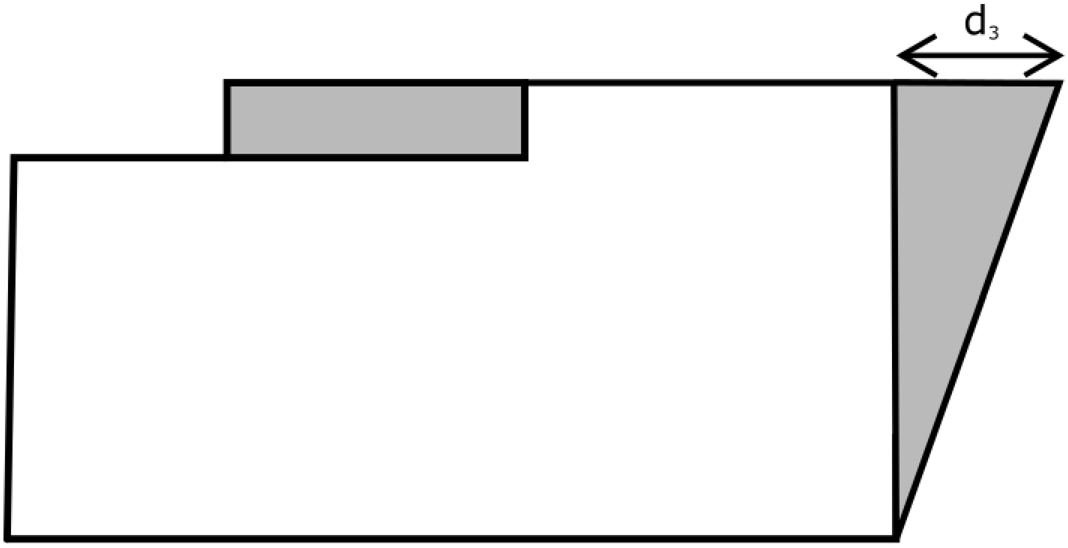

Figure 5.2: Wetted surface of the first variant of the BBDB geometry. $d_3 = 6.13m$

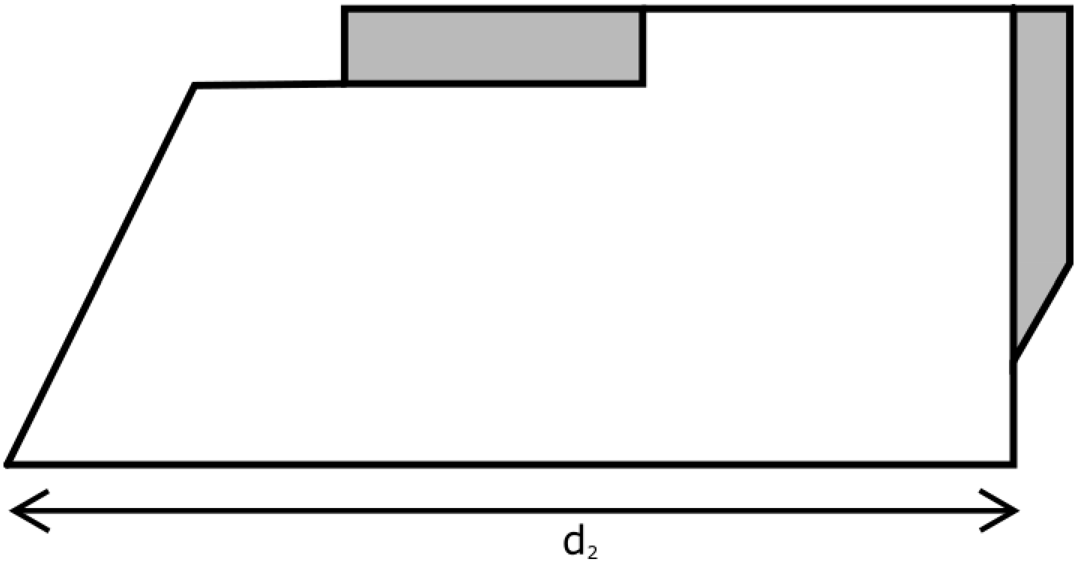

Figure 5.3: Wetted surface of the second variant of the BBDB geometry. $d_2 = 40.87m$

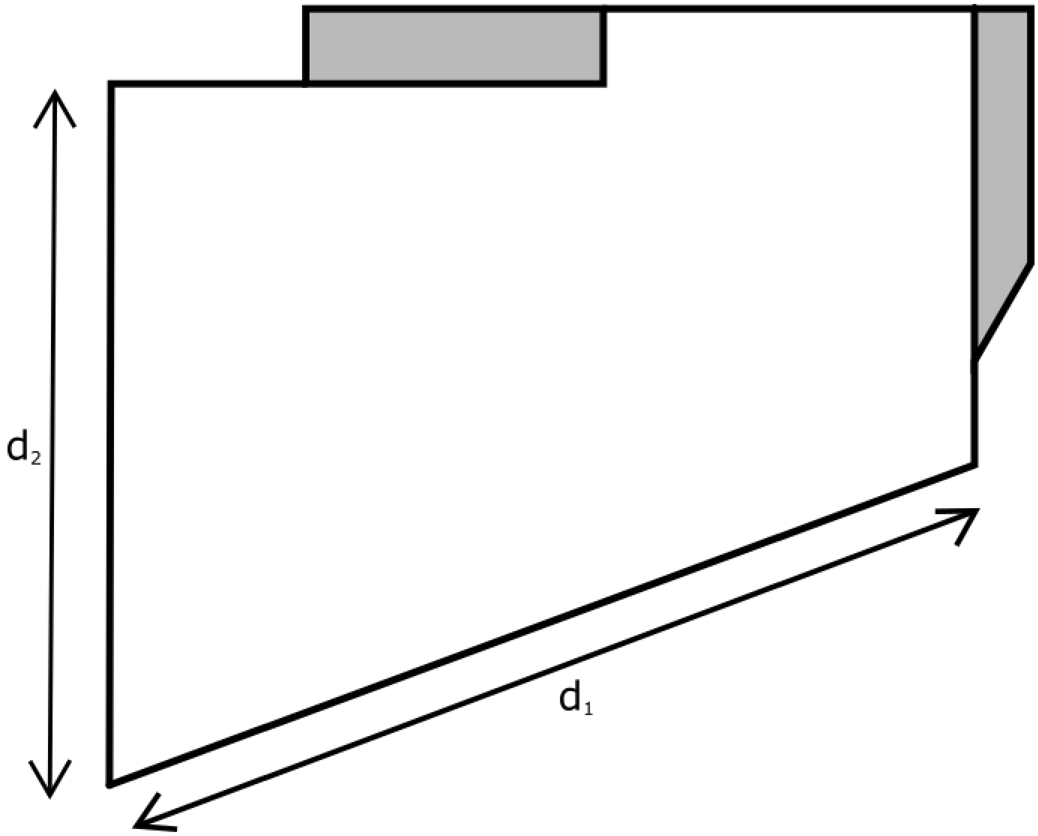

Figure 5.4: Wetted surface of the third variant of the BBDB geometry. $d_1 = 36.4m$ and $d_2 = 24m$

FlOWCITSS simulates all geometries using the same mooring configuration. The mooring line is a simple catenary mooring chain whose characteristics are detailed in Table 5.1. The mooring line is anchored at the same point on every BBDB: the bottom corner opposite the opening of the OWC. The anchor placement on the bottom of the ocean is defined relative to the anchor point on the body. FlOWCITSS also uses the same drag coefficients and turbine loading resistance for all geometries, the details of which are presented in Table 5.1.

Table 5.1: Simulation and Mooring Parameters

| Characteristics | Values |
|---|---|
| Line Length | 730 m |
| Anchor Depth | 400 m |
| $x$ Distance from body | 600 m |
| Mass per Unit Length | 90 $\frac{kg}{m}$ |
| Heave mooring Damping | 90 $\frac{Ns}{m}$ |
| Surge mooring Damping | 60 $\frac{Ns}{m}$ |
| Pitch mooring Damping | 900 $\frac{Ns}{\text{deg}}$ |
| Turbine Loading Resistance | 30$\frac{kg}{m^4 s}$ |
| Surge Drag Coefficient | 2.5 |
| Heave Drag Coefficient | 5.0 |

The incident waves of interest are monochromatic linear waves of of the form $\eta = A\cos\omega t$, where $\eta$ is the wave elevation, $A$ is the wave amplitude and $\omega$ is the frequency. The wave amplitude of interest is 1.5 m. FlOWCITSS evaluates for 2 different periods: 9 seconds and 3 seconds.

## 5.2 Performance and Time Domain Response

### 5.2.1 9 Second Wave Period

For this incident wave, FlOWCITSS was tested with different solvers and time steps in SimuLink. For solvers, both fixed-step implicit and fixed-step explicit solvers were tested, and time step size ranged from 0.001 seconds to 0.00001 seconds. All geometries but RM6 were unable to converge, and RM6 was able to converge only after adjusting the mooring parameters and testing multiple solvers. RM6 was able to converge using ode3 in Simulink, with a time step size of 0.0002 seconds. The steady state power performance of RM6 is shown in Figure 5.5.

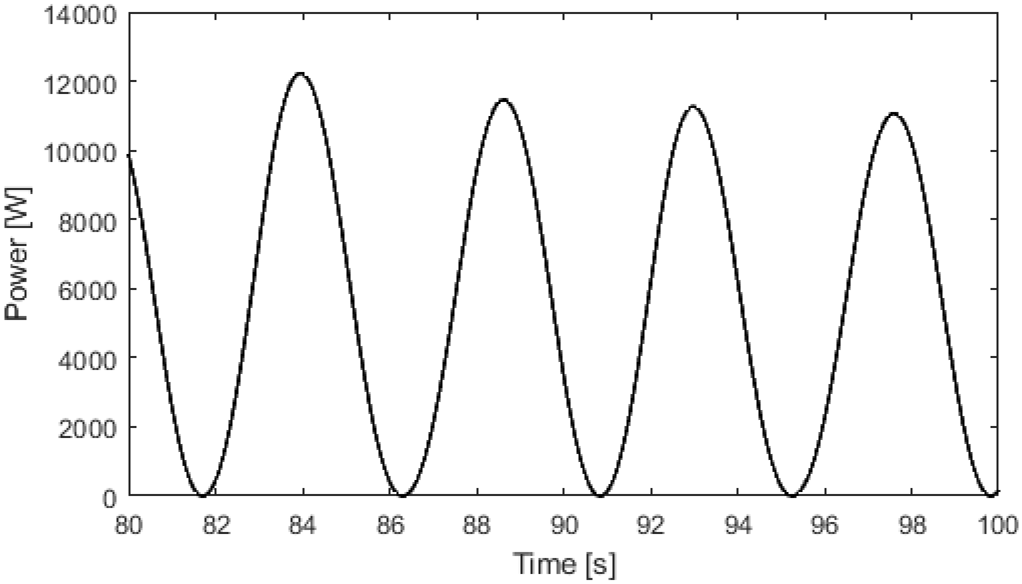

Figure 5.5: RM6 steady state response to the incident wave with a 9 second period.

The convergence issue could come from FlOWCITSS dealing with larger displacements and pressures than were previously tested in the validation section.

### 5.2.2 3 Second Wave Period

For this incident wave, FlOWCITSS used the fixed-step ode3 solver in SimuLink with a time step ranging from 0.0002 seconds to 0.00001 seconds. All geometries were able to converge in this wave environment, and the steady state pneumatic power is shown in Figure 5.6.

The power generation seen in Figure 5.6 is different for each geometry. The largest response comes from RM6, with a peak value of around 5 kW. The smallest response comes from the second BBDB variant, which is out of phase from the rest of the geometries and has a peak power output of around 2 kW. When comparing the RM6 power output of this incident wave to the 9 second period incident wave, they vary not only in frequency, but also in magnitude.

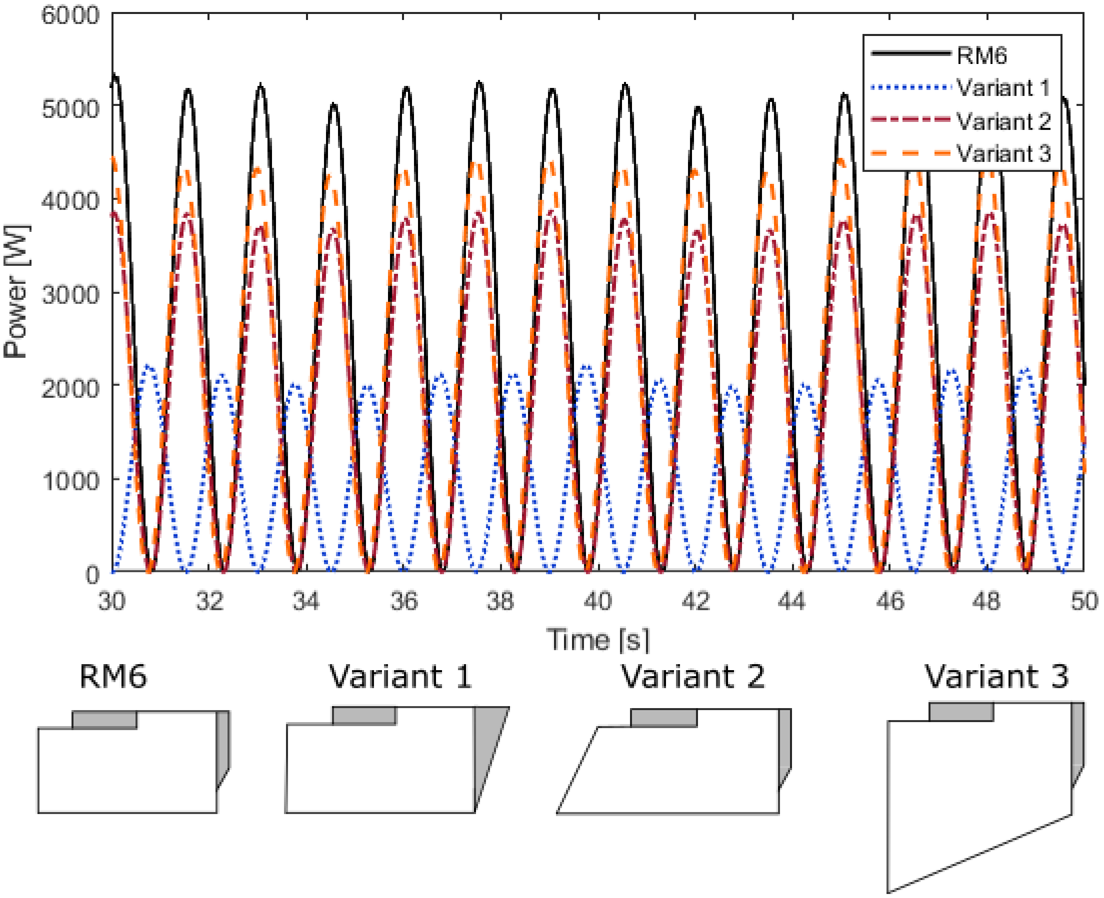

Figure 5.6: Steady state power performance plot for an incident wave with with a 3 second period.

The geometry with the most notable departure in performance from RM6 is Variant 1, with the altered stern geometry. Variant 1 not only has a response of decreased magnitude, but also one that is out of phase from the other geometries. This indicates that stern geometry in particular significantly impacts the power output and would warrant further investigation.

## 5.3 Discussion

These variations in power generation between different geometries and different wave environments demonstrate the usefulness of FlOWCITSS as a tool. Given the errors witnessed in the previous chapter, FlOWCITSS would be ideal to identify those geometries that have significantly better, or worse, performance than the others. For example, in Figure 5.6, the first BBDB variant has a peak power of less than half of RM6. FlOWCITSS is useful here in identifying the first variant's poor power performance compared to RM6 due to the large discrepancy between the two. FlOWCITSS would be less useful in distinguishing between the power performance of the second and third variants, since they have a difference in peak magnitude closer to 500 W, which is approximately a 12% difference, and is within the error FlOWCITSS demonstrated when compared to physical experiments.

This investigation of the BBDB archetypes has also illuminated other areas where FlOWCITSS could improve: primarily in the robustness of the tool and its ability to handle a wide variety of geometries for all wave conditions. Based on the convergence issues with a wave environment that would produce a large response for large scale WECs, it appears that FlOWCITSS in its current iteration would be better suited to smaller floating OWCs.

# Chapter 6

# Conclusions

This thesis has presented the implementation and testing of an open access time domain modeling tool for floating OWCs. This final chapter will conclude the thesis with a brief summary of the presented work, a list of the contributions of the research, and a recommendation for possible future work.

## 6.1 Brief Summary of Thesis

Chapter 1 introduced floating OWCs and explained the motivation behind the open access time domain modeling tool. While programs do exist that model floating OWCs in the time domain, they can be expensive and they do not use the pressure distribution model. The pressure distribution model, in theory, accounts for the internal water column motion better than the piston model for large scale devices. Additionally, an open access time domain modeling tool allows for a user to evaluate many floating OWC configurations and select the ones that look most promising for further exploration with higher fidelity methods, such as CFD. An example of where this tool can be used is in the exploration of the BBDB archetype's hull geometry.

Next, chapter 2 outlined the process of synthesizing the mathematical model and explained why certain models are used. Using superposition, basic body forcing and volume flow equations can be enhanced by considering additional body forces or volume flow effects.

Some of the effects considered are drag, air compressibility, mooring, and hydrostatic forces.

Chapter 3 explained how the mathematical model is represented by a block diagram and how FlOWCITSS is implemented to evaluate floating OWCs in the time domain. To avoid convolution integration, state space realization of the FRFs is used and demonstrated for the pressure distribution FRFs. The block diagram has several subsystems, one for each volume flow and body forcing equation, one for the mooring model, and one to account for air compressibility and turbine dynamics. The outputs of SimuLink are the body motion in all directions, the chamber pressure, and the volume flow across the turbine. The chamber pressure and volume flow across the turbine are used to estimate the pneumatic power.

Chapter 4 compared simulated results from FlOWCITSS to experimental results. Two test cases were used for each geometry, one to tune unknown parameters, and one to test the adequacy of the tuned parameters. Although FlOWCITSS demonstrated significant error for some aspects of the device response, FlOWCITSS did capture the general oscillatory nature and the period of the response for heave motions, with varying error in the magnitude. It is able to analyze a variety of geometries and is useful for estimating device performance as a preliminary discovery step to higher fidelity techniques, such as CFD.

Finally, chapter 5 demonstrated the use of the tool by simulating the time domain response of RM6 and several geometry variations of the BBDB archetype to compare device performance under the same conditions. Some geometries had trouble with converging solutions for the 9 second wave period, but all solutions were found for the 3 second wave period. The power performance of each device was different, with the largest difference in performance happening between RM6 and the geometry variation using an alternative stern geometry. The significant phase difference and magnitude indicates that stern geometry can have a large impact on power generation. The ability for FlOWCITSS to estimate power generation for a variety of geometries without the use of time consuming proprietary codes can open the door for a more comprehensive investigation of floating OWC geometry. Additionall, it can benefit the research community by providing an inexpensive time domain modelling tool for this WEC archetype.

## 6.2 Contributions

This thesis has several contributions. The predominant contribution is the creation of an open-access time domain modeling tool for floating OWCs. The creation of this tool also involved selecting appropriate models for different physical effects and determining what physical effects to take into account. Additionally, this body of work uses the pressure distribution model, something that other time domain modeling tools do not consider. In this pressure distribution model, unique FRFs appear, and this thesis demonstrated the adequacy of the state space representation to circumvent convolution integration for these FRFs. Finally, this thesis demonstrated the use of this tool by exploring several BBDB geometries for a wave condition.

## 6.3 Recommendations for Future Work

FlOWCITSS as a tool has a lot of potential directions for future work. In order to get a better idea of the error associated with simulations using FlOWCITSS, the tool could be compared to an experiment with fewer uncertainties and unknowns.

Several aspects of the mathematical model could be refined. The mooring model could be improved by considering a nonlinear damping relationship, instead of the linear relationship that FlOWCITSS currently assumes. Additionally, the drag estimation could be refined by more carefully considering the variation of the fluid velocity across the surface of the body. Furthermore, the calculation of the inputs could be expanded to include irregular, polychromatic waves. This would allow for users to simulate more realistic wave conditions and obtain a better of understanding of how a WEC would perform in an actual ocean.

The implementation of FlOWCITSS could be further improved by making it more robust or efficient. Ideally, all geometries would be able to be simulated for all realistic wave conditions, and increased efficiency or robustness would help achieve that goal.

# Bibliography

[1] Aurélien Babarit. *Ocean wave energy conversion : resource, technologies and performance*. ISTE Press Elsevier Ltd, London, UK Oxford, UK, 2017. ISBN 9780081023907.

[2] Helen Bailey, Bryson R.D. Robertson, and Bradley J. Buckham. Wave-to-wire simulation of a floating oscillating water column wave energy converter. *Ocean Engineering*, 125:248–260, oct 2016. doi: 10.1016/j.oceaneng.2016.08.017.

[3] D. Bull and P. Jacob. Methodology for creating nonaxisymmetric wecs to screen mooring designs using a morison equation approach. In *2012 Oceans*, pages 1–9, 2012.

[4] Diana Bull, Chris Smith, Dale Scott Jenne, Paul Jacob, Andrea Copping, Steve Willits, Arnold Fontaine, Dorian Brefort, Guild Copeland, Margaret Gordon, et al. Reference model 6 (rm6): Oscillating wave energy converter. *Report by Sandia National Laboratories (SNL)*, 2014.

[5] Diana Bull, D. Scott Jenne, Christopher S. Smith, Andrea E. Copping, and Guild Copeland. Levelized cost of energy for a backward bent duct buoy. *International Journal of Marine Energy*, 16:220–234, dec 2016. doi: 10.1016/j.ijome.2016.07.002.

[6] W. E. Cummins. The impulse response function and ship motions. *Symposium on Ship Theory*, 9:101–109, 1962. URL `www.scopus.com`. Cited By :31.

[7] Josh Davidson and John V. Ringwood. Mathematical modelling of mooring systems for wave energy converters—a review. *Energies*, 10(5):666, may 2017. doi: 10.3390/en10050666.

[8] António F. de O. Falcão. Wave energy utilization: A review of the technologies. *Renewable and Sustainable Energy Reviews*, 14(3):899–918, apr 2010. doi: 10.1016/j.rser.2009.11.003.

[9] D. Deschrijver, M. Mrozowski, T. Dhaene, and D. De Zutter. Macromodeling of multiport systems using a fast implementation of the vector fitting method. *IEEE Microwave and Wireless Components Letters*, 18(6):383–385, jun 2008. doi: 10.1109/lmwc.2008.922585.

[10] *Recommended Practice DNV-RP-C205 Environmental Conditions and Environmental Loads*. Det Norske Veritas, October 2010.

[11] D. V. EVANS. The oscillating water column wave-energy device. *IMA Journal of Applied Mathematics*, 22(4):423–433, 1978. doi: 10.1093/imamat/22.4.423.

[12] D.V. Evans and R. Porter. Hydrodynamic characteristics of an oscillating water column device. *Applied Ocean Research*, 17(3):155–164, jun 1995. doi: 10.1016/0141-1187(95)00008-9.

[13] J. Falnes. *Ocean Waves and Oscillating Systems: Linear Interactions Including Wave-Energy Extraction*. Cambridge University Press, 2002. ISBN 9781139431934. URL `https://books.google.com/books?id=bl1FyQjCklgC`.

[14] L.O. Garza-Rios, M.M. Bernitsas, and K. Nishimoto. Catenary mooring lines with nonlinear drag and touchdown. Technical report, University of Michigan/Industry Consortium in Offshore Engineering, 1997.

[15] B. Gustavsen. Improving the pole relocating properties of vector fitting. *IEEE Transactions on Power Delivery*, 21(3):1587–1592, jul 2006. doi: 10.1109/tpwrd.2005.860281.

[16] B. Gustavsen and A. Semlyen. Rational approximation of frequency domain responses by vector fitting. *IEEE Transactions on Power Delivery*, 14(3):1052–1061, jul 1999. doi: 10.1109/61.772353.

[17] Gabriele C. Hegerl and Ulrich Cubasch. Greenhouse gas induced climate change. *Environmental Science and Pollution Research*, 3(2):99–102, jun 1996. doi: 10.1007/bf02985499.

[18] Paul T Jacobson, George Hagerman, and George Scott. Mapping and assessment of the united states ocean wave energy resource. Technical report, Electric Power Research Institute, 12 2011.

[19] E.R. Jefferys. Simulation of wave power devices. *Applied Ocean Research*, 6(1):31–39, jan 1984. doi: 10.1016/0141-1187(84)90026-9.

[20] L Johanning and GH Smith. Improved measurement technologies for floating wave energy converter (WEC) mooring arrangements. *Underwater Technology*, 27(4):175–184, jun 2008. doi: 10.3723/ut.27.175.

[21] Lars Johanning, George H. Smith, and Julian Wolfram. Measurements of static and dynamic mooring line damping and their importance for floating WEC devices. *Ocean Engineering*, 34(14-15):1918–1934, oct 2007. doi: 10.1016/j.oceaneng.2007.04.002.

[22] Bi jun Wu, Meng Li, Ru kang Wu, Yun qiu Zhang, and Wen Peng. Experimental study on primary efficiency of a new pentagonal backward bent duct buoy and assessment of prototypes. *Renewable Energy*, 113:774–783, dec 2017. doi: 10.1016/j.renene.2017.06.010.

[23] Adi Kurniawan, Jorgen Hals, and Torgeir Moan. Modelling and simulation of a floating

oscillating water column. In *Volume 5: Ocean Space Utilization: Ocean Renewable Energy*. ASME, 2011. doi: 10.1115/omae2011-49263.

[24] Adi Kurniawan, Jørgen Hals, and Torgeir Moan. Assessment of time-domain models ofwave energy conversion systems. In *Proceedings of the 9th European Wave and Tidal Energy Conference (EWTEC 2011)*, 2011.

[25] Y. Masuda, T. Yamazaki, Y. Outa, and M. E. McCormick. The backward bend duct buoy-an improved floating type wave power device. In *OCEANS '88. 'A Partnership of Marine Interests'. Proceedings*, pages 1067–1072 vol.3, 1988.

[26] J. N. Newman. *Marine hydrodynamics*. MIT Press, Cambridge, Mass, 1977. ISBN 9780262280617.

[27] J. N. Newman and C.-H. Lee. Boundary-element methods in offshore structure analysis. *Journal of Offshore Mechanics and Arctic Engineering*, 124(2):81–89, apr 2002. doi: 10.1115/1.1464561.

[28] De-Zhi Ning, Jin Shi, Qing-Ping Zou, and Bin Teng. Investigation of hydrodynamic performance of an OWC (oscillating water column) wave energy device using a fully nonlinear HOBEM (higher-order boundary element method). *Energy*, 83:177–188, apr 2015. doi: 10.1016/j.energy.2015.02.012.

[29] Koji Ohta and Hatsuo Ishida. Comparison among several numerical integration methods for kramers-kronig transformation. *Applied Spectroscopy*, 42(6):952–957, aug 1988. doi: 10.1366/0003702884430380.

[30] Markel Penalba, Giussepe Giorgi, and John V. Ringwood. Mathematical modelling of wave energy converters: A review of nonlinear approaches. *Renewable and Sustainable Energy Reviews*, 78:1188–1207, oct 2017. doi: 10.1016/j.rser.2016.11.137.

[31] Markel Penalba, Thomas Kelly, and John Ringwood. Using nemoh for modelling wave energy converters: A comparative study with wamit. In *12th European Wave and Tidal Energy Conference (EWTEC)*, 2017. URL http://mural.maynoothuniversity.ie/12466/.

[32] Tristan Perez and Thor Inge Fossen. A matlab toolbox for parametric identification of radiation-force models of ships and offshore structures. *Modeling, Identification and Control: A Norwegian Research Bulletin*, 30(1):1–15, 2009. doi: 10.4173/mic.2009.1.1.

[33] J.C.C. Portillo, P.F. Reis, J.C.C. Henriques, L.M.C. Gato, and A.F.O. Falcão. Backward bent-duct buoy or frontward bent-duct buoy? review, assessment and optimisation. *Renewable and Sustainable Energy Reviews*, 112:353 – 368, 2019. ISSN 1364-0321. doi: https://doi.org/10.1016/j.rser.2019.05.026. URL http://www.sciencedirect.com/science/article/pii/S1364032119303387.

[34] Robert A. Dalrymple Robert G. Dean. *Water Wave Mechanics for Engineers and Scientists*. WORLD SCIENTIFIC PUB CO INC, 1991. ISBN 9810204213. URL https://www.ebook.de/de/product/6958988/robert_g_dean_robert_a_dalrymple_water_wave_mechanics_for_engineers_and_scientists.html.

[35] A. J. N. A. Sarmento and A. F. de O. Falcão. Wave generation by an oscillating surface-pressure and its application in wave-energy extraction. *Journal of Fluid Mechanics*, 150:467–485, 1985. doi: 10.1017/S0022112085000234.

[36] Wanan Sheng. Power performance of BBDB OWC wave energy converters. *Renewable Energy*, 132:709–722, mar 2019. doi: 10.1016/j.renene.2018.07.111.

[37] Wanan Sheng. Motion and performance of BBDB OWC wave energy converters: I, hydrodynamics. *Renewable Energy*, 138:106–120, aug 2019. doi: 10.1016/j.renene.2019.01.016.

[38] Wanan Sheng, Raymond Alcorn, and Anthony Lewis. On thermodynamics in the primary power conversion of oscillating water column wave energy converters. *Journal of Renewable and Sustainable Energy*, 5(2):023105, mar 2013. doi: 10.1063/1.4794750.

[39] R. So, B. Bosma, K. Ruehl, and T. K. A. Brekken. Modeling of a wave energy oscillating water column as a point absorber using wec-sim. *IEEE Transactions on Sustainable Energy*, 11(2):851–858, 2020.

[40] Gilbert Strang. *Calculus*. Cambridge University Pr., 2017. ISBN 0980232759. URL `https://www.ebook.de/de/product/30266796/gilbert_strang_calculus.html`.

[41] Masami Suzuki, Toshiari Kuboki, Shuichi Nagata, and Toshiaki Setoguchi. Numerical Investigation of 2D Optimal Profile of Backward-Bent Duct Type Wave Energy Converter. *Journal of Offshore Mechanics and Arctic Engineering*, 133(4), 04 2011. ISSN 0892-7219. doi: 10.1115/1.4003519. URL `https://doi.org/10.1115/1.4003519`. 041602.

[42] Kazutaka TOYOTA, Shuichi NAGATA, Yukitaka IMAI, and Toshiaki SETOGUCHI. Effects of hull shape on primary conversion characteristics of a floating owc rdquo;backward bent duct buoyrdquo;. *Journal of Fluid Science and Technology*, 3 (3):458–465, 2008. doi: 10.1299/jfst.3.458.

[43] *WAMIT User Manual*. WAMIT, Incorporated and Massachusetts Institute of Technology, 822 Boylston St. – Suite 202 Chestnut Hill, MA 02467-2504, 2019. URL `wamit.com`.

[44] Y. Washio, H. Osawa, and T. Ogata. The open sea tests of the offshore floating type wave power device ”mighty whale” -characteristics of wave energy absorption and power generation. In *MTS/IEEE Oceans 2001. An Ocean Odyssey. Conference Proceedings (IEEE Cat. No.01CH37295)*. Marine Technol. Soc, 2001. doi: 10.1109/oceans.2001.968786.

[45] James H. Williams, Andrew DeBenedictis, Rebecca Ghanadan, Amber Mahone, Jack Moore, William R. Morrow, Snuller Price, and Margaret S. Torn. The technology path to deep greenhouse gas emissions cuts by 2050: The pivotal role of electricity. *Science*, 335 (6064):53–59, 2012. ISSN 00368075, 10959203. URL `http://www.jstor.org/stable/41487099`.

[46] Minghao Wu, Vasiliki Stratigaki, Peter Troch, Corrado Altomare, Tim Verbrugghe, Alejandro Crespo, Lorenzo Cappietti, Matthew Hall, and Moncho Gómez-Gesteira. Experimental study of a moored floating oscillating water column wave-energy converter and of a moored cubic box. *Energies*, 12(10):1834, May 2019. ISSN 1996-1073. doi: 10.3390/en12101834. URL `http://dx.doi.org/10.3390/en12101834`.

# Appendices

# Appendix A

# First Appendix

## A.1 GitHub Repository

Here is the link where the MatLab script, block diagram, and user guide are published and publicly accessible: https://github.com/wendelleS/FlOWCITSS